

Novel exact black hole solution in Dehnen $\left(1, 4, \frac{3}{2}\right)$ halo: thermodynamics, photon circular motion and eikonal quasinormal modes

David Senjaya¹, Thanaporn Chuensuksan², Supakchai Ponglertsakul³

¹Department of Physics, Faculty of Science, Mahidol University, Bangkok 10400, Thailand.

²Department of Physics, Faculty of Science, Srinakharinwirot University, Bangkok 10110, Thailand.

³Strong Gravity Group, Department of Physics, Faculty of Science, Silpakorn University, Nakhon Pathom 73000, Thailand.

Contributing authors: davidsenjaya@protonmail.com;
thanapornchnsksn@gmail.com; supakchai.p@gmail.com;

Dehnen $\left(1, 4, \frac{3}{2}\right)$ dark matter halo has been proven to be a valuable model for describing the surface brightness distributions of elliptical galaxies, yet its implications for black hole spacetimes remain largely unexplored. In this work, we construct a novel exact black hole solution embedded in this Dehnen halo and investigate its physical consequences. The influence of the halo on black hole thermodynamics is analyzed through the mass function, entropy, Hawking temperature, heat capacity, and Gibbs free energy, allowing us to assess both local and global thermodynamic stability of the black hole–dark matter system. Our results show that the presence of a Dehnen-type halo not only stabilizes the otherwise thermodynamically unstable Schwarzschild black hole but also induces phase transitions. In addition, we study null geodesics to examine photon motion, the shadow radius and the optical appearance of the system. The dark matter halo modifies the effective potential, leading to observable changes in the photon sphere and the apparent size of the shadow. We also explore the instability of circular null geodesics and its relation to quasinormal modes in an eikonal limit. These findings highlight the significant role of realistic dark matter distributions in shaping both the thermodynamic behavior and the observable signatures of

black holes, providing further insight into the interplay between dark matter halos and central black holes in galaxies.

1 Introduction

Despite extensive testing, Einstein's General Relativity cannot fully explain black hole singularities, dark matter and dark energy. Although gravitational waves and black holes' shadow images from the Event Horizon Telescope [1–3] confirm the prediction of black holes, the theory is still considered incomplete. Among the remaining problems in general relativity, dark matter stands as one of the most profound and persistent mysteries, challenging our understanding of the universe. Its existence can be inferred from various astrophysical and cosmological observations, including galaxy rotation curves [4], gravitational lensing [5], the cosmic microwave background [6] and collision of galaxy clusters [7, 8].

On the galactic scales, dark matter plays a crucial role in stellar dynamics around galaxies. For instance, the fact that galactic rotation curves stay flat for big galaxies prompted the dark matter theory to explain the invisible mass. An astronomical research reveals that the rotating movements of stars in these galaxies can only be explained by dark matter [9], which might account for up to 90 percent [10, 11] of a galaxy's total mass, whereas the remainder made up of conventional baryonic matter. Moreover, during the early phases of the universe, dark matter collected around galactic centers to promote star formation. As the galaxies developed to reach their mature stage, dark matter drifted outward, generating halos. An advancement of astrophysical instruments reveals that there are evidences that most galaxies are surrounded by dark matter halo stretching far beyond a visible part of galaxies [12]. Moreover, recent observations have confirmed existence of supermassive black hole at the centre of galaxy *M87** [2] and the Milky Way galaxy [3].

Black holes embedded in dark matter environments provide a natural laboratory to explore the mutual interaction between black holes and dark matter. With the presence of dark matter, the gravitational field of black hole is modified. This could potentially leave imprints on observable quantities such as black hole shadows, gravitational lensing and the motion of test particles. In recent years, there has been many interests in finding black hole solutions embedded in various dark matter halo profiles. A rotating black hole surrounded by Universal Rotation Curve dark matter profile is constructed. Shadow's radius of such a Kerr-like solution is found to be smaller than those of the Kerr black hole [13] given the core radius is comparable to the mass of black hole and very high core's density. By using several dark matter profiles such as Navarro-Frenk-White, Burkert and Hernquist as source of energy-momentum tensor, the authors of [14] solve the Einstein field equation and find the spacetime metrics representing black holes embedded in galactic halos. For cold dark matter Einasto profile, exact and numerical black hole solutions are explored in [15, 16]. Shadow and gravitational lensing of Schwarzschild black hole embedded in the Hernquist profile is significantly different from the Schwarzschild vacuum solution [17, 18]. More interestingly, a suitable incorporation of dark matter halos allows one to construct regular black hole solutions [19].

A Dehnen profile is flexible model which can give rise to either cored or cuspy profile. It was originally developed to describe mass distribution in galaxies [20]. In particular, it is commonly applied to dwarf galaxies. In general, dwarf galaxies do not host black hole at their centre. But some recent observations indicate a possibility of supermassive black holes hosted by *Mrk 462*, *Henize 2 – 10* and *Leo I* [21–23]. A particular class of dwarf galaxy called ultra fainted dwarf galaxies usually contain very old and long-lived stars. Therefore, it is one of the least luminosity known galaxy. Consequently, it has the highest dark matter to light ratio. Hence, it is a perfect place to explore nature of dark matter. In 2022, rotating black hole immersed in the Dehnen halo is constructed and its shadow properties are investigated [24]. To distinguish dark matter profile whether it is cored or cuspy, weak deflection angle provides a much better way to differentiate dark matter profile as reported in [24]. This work has sparked interest and led to many studies devoted to black hole solutions surrounded by various Dehnen dark matter profiles [25–29].

In this work, we use the approach introduced in [30] to derive a new static spherically symmetric black hole solution immersed in the Dehnen-type $(1, 4, \frac{3}{2})$ density profile describing dark matter halo. The Dehnen $(1, 4, \frac{3}{2})$ profile has proven to be a valuable tool in modeling the surface brightness distribution of elliptical galaxies [26, 31]. Specifically, the choice of $\gamma = 3/2$ (see (7) below) shows the most resemblance to the de Vaucouleurs's surface brightness profile [20]. Despite its success in capturing the observed stellar density structures, a corresponding analytical black hole solution within this framework remains unexplored. Investigating such a solution is essential, as it would provide deeper insights into the interplay between galactic density profiles and central compact objects, thereby bridging a critical gap between astrophysical modeling and gravitational theory.

This article is organized as follow. In section 2, we construct an exact static spherically symmetric black hole surrounded by the Dehnen $(1, 4, \frac{3}{2})$ density profile. Then, the singularity structure and energy conditions are investigated. Thermodynamics quantities such as temperature, heat capacity and free energy of the solution in section 3. In section 4, we analyze geodesics of massless particle around the black holes. Black hole's shadow radius is computed and compared with observational data. In section 5, we explore instability of circular null orbit via Lyapunov exponent. Quasinormal frequencies in eikonal limit are derived in section 6. We summarize our findings in the last section 7.

2 Black hole + DM profile

To construct the spacetime metric describing black hole immersed in dark matter halo, we follow the method that is outlined in [30]. We start by considering a static spherically symmetric black hole surrounded by dark matter halo. The general metric is given by

$$ds^2 = -[f(r) + F(r)] dt^2 + [g(r) + G(r)]^{-1} dr^2 + r^2 (d\theta^2 + \sin^2 \theta d\phi^2), \quad (1)$$

where throughout this work, we have set $c = G = 1$. In an absence of black hole, i.e., $F = G = 0$, the spacetime background above reduces to pure dark matter spacetime.

The energy-momentum tensor solely comes from the presence of dark matter halo. Therefore, the Einstein field equation can be written as

$$R_a^b + \frac{1}{2}R\delta_a^b = 8\pi T_a^b, \quad (2)$$

where $T_a^b = \text{diag}[-\rho_E, p_r, p, p]$. represents energy momentum tensor of dark matter. The independent components of the Einstein field equation are

$$8\pi T_t^t = \frac{(-1 + g + G)}{r^2} + \frac{(g + G)'}{r}, \quad (3)$$

$$8\pi T_r^r = (g + G) \left[\frac{(f + F)'}{r(f + F)} + \frac{1}{r^2} \right] - \frac{1}{r^2}, \quad (4)$$

$$\begin{aligned} 8\pi T_\theta^\theta &= \frac{(g + G)}{2(f + F)} \left[(f + F)'' - \frac{(f + F)'}{2(f + F)} + \frac{(f + F)'}{r} \right] \\ &\quad + (g + G)' \left[\frac{(f + F)'}{4(f + F)} + \frac{1}{2r} \right], \end{aligned} \quad (5)$$

where prime denotes derivative with respect to r . Without dark matter halo, i.e., vanishing energy momentum tensor and $f = g = 1$, the above equations admit the Schwarzschild solution. Thus, we obtain

$$F = G = -\frac{r_s}{r}, \quad (6)$$

where $r_s = 2M$ with M being the Schwarzschild mass.

In this work, we are interested in the Dehnen type dark matter halo [20], having the following form of mass density,

$$\rho(r) = \rho_0 \left(\frac{r}{r_0} \right)^{-\gamma} \left(1 + \left(\frac{r}{r_0} \right)^\alpha \right)^{\frac{\gamma-\beta}{\alpha}}. \quad (7)$$

We specifically choose $(\alpha, \beta, \gamma) = (1, 4, \frac{3}{2})$ such that the Dehnen profile matches the de Vaucouleurs's law ($r^{1/4}$ law). This yields the following explicit expression,

$$\rho(r) = \rho_0 \left(\frac{r}{r_0} \right)^{-\frac{3}{2}} \left(1 + \frac{r}{r_0} \right)^{-\frac{5}{2}}, \quad (8)$$

where ρ_0 is a constant acting as the dark matter halo central density parameter and r_0 is halo core radius [25]. In spherically symmetric spacetime, the mass distribution function can be calculated by [32]

$$M_{DM} = 4\pi \int_0^r \rho(\hat{r}) \hat{r}^2 d\hat{r} = \frac{8}{3}\pi \rho_0 r_0^3 \left(1 + \frac{r_0}{r} \right)^{-\frac{3}{2}}. \quad (9)$$

It is clear that the dark matter mass profile depends on the central density ρ_0 and halo's core radius r_0 . A test particle moving under an influence of dark matter has a tangential velocity that relates to the mass distribution (9)

$$v_t(r) = \sqrt{\frac{M_{DM}(r)}{r}} = \sqrt{\frac{8}{3}\pi\rho_0 r_0^3} \left(1 + \frac{r_0}{r}\right)^{-\frac{3}{4}} r^{-\frac{1}{2}}. \quad (10)$$

In a pure dark matter spacetime, i.e., $F = G = 0$, the tangential velocity relates to the red shift function of the spacetime metric f [30]

$$v_t^2(r) = r \frac{d}{dr} \left(\ln \sqrt{f(r)} \right), \quad (11)$$

where we impose $f = g$. Thus, we can solve for the redshift function

$$\begin{aligned} f(r) &= e^{2 \int \frac{v_t^2(r)}{r} dr}, \\ &= e^{\frac{32}{3}\pi\rho_0 r_0^2 \left(1 + \frac{r_0}{r}\right)^{-\frac{3}{2}}}. \end{aligned} \quad (12)$$

Note that, the central density ρ_0 can be re-written in term of dark matter mass M_{DM} via (9). Therefore, a static spherically symmetric spacetime describing a black hole surrounded by a dark matter halo with Dehnen type $(1, 4, \frac{3}{2})$ can be written explicitly as

$$ds^2 = - \left(e^{4M_{DM} \left(\frac{1}{r} + \frac{1}{r_0} \right)} - \frac{r_s}{r} \right) dt^2 + \frac{dr^2}{\left(e^{4M_{DM} \left(\frac{1}{r} + \frac{1}{r_0} \right)} - \frac{r_s}{r} \right)} + r^2 (d\theta^2 + \sin^2 \theta d\phi^2). \quad (13)$$

We notice that $g_{tt} \rightarrow e^{4M_{DM}/r_0}$ as $r \rightarrow \infty$, which is clearly constant. Moreover, in the absence of dark matter $M_{DM} = 0$, the metric above reduces to the standard form of the Schwarzschild metric. For theoretical purposes, we shall fix black hole mass $M = 1$ throughout this study, unless otherwise stated.

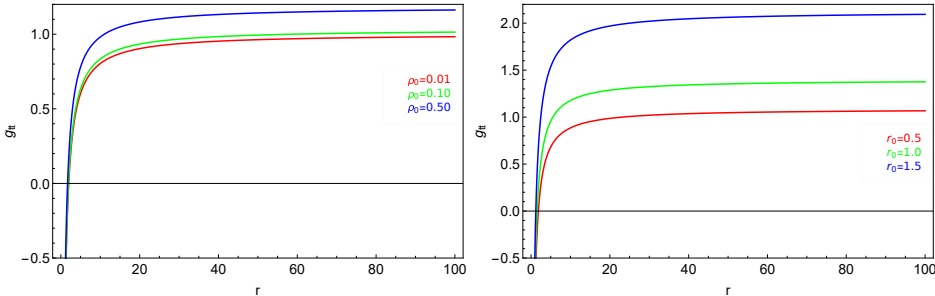


Fig. 1 Metric function g_{tt} as a function of r for $r_s = 2$. Left: fixed $r_0 = 0.1$, Right: fixed $\rho_0 = 0.01$.

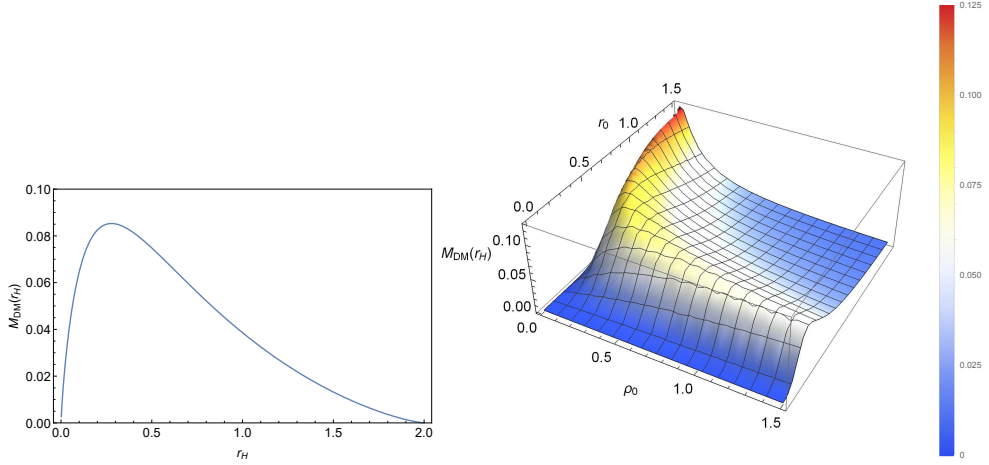


Fig. 2 Left: $M_{DM}(r_H)$ as a function of r_H . Right: 3D plot of $M_{DM}(r_H)$ as a function of ρ_0 and r_0 .

In Fig. 1, we display behavior of the metric function g_{tt} as a function of r . It can be clearly seen that g_{tt} approaches a constant value at large r . The location of the black hole's event horizon can be determined from the zero of g_{tt} . For instance, the event horizon locates at $r = r_H = 1.857$ for $\rho_0 = 0.01$ and $r_0 = 0.5$.

The left panel of Fig. 2 demonstrates the value of the dark matter halo mass at the horizon $M_{DM}(r_H)$ plotting against the radius of the horizon r_H . Recall that, $M_{DM}(r_H)$ and r_H depend explicitly on ρ_0, r_0 . Therefore, for the sake of demonstration, we set $\rho_0 = r_0$ in this plot. We observe that the dark matter mass reaches its maximum at $r_H = 0.27$ and $M_{DM}(r_H) = 0.085$. After $r_H > 0.27$, the dark matter halo mass at the horizon decreases monotonically with r_H . In the right panel of Fig. 2, we depict how $M_{DM}(r_H)$ is influenced by the central dark matter energy density ρ_0 and the core's radius r_0 . Interestingly, the maximum mass attains at small ρ_0 and large r_0 .

Now let us investigate the existence of singularity with the presence of dark matter halo. Here, we explore the Ricci scalar (R), Ricci scalar square $R_{ab}R^{ab}$ and the Kretschmann scalar $R_{abcd}R^{abcd}$. For the given metric (1), these are explicitly obtained

$$R = \frac{2(1-f-F)}{r^2} - \frac{4(f+F)'}{r} - (f+F)'' , \quad (14)$$

$$R_{ab}R^{ab} = 4 \left[\frac{(f+F-1)^2}{2r^4} + \frac{(f+F-1)(f+F)'}{r^3} + \frac{(f+F)'^2}{r^2} \right. \\ \left. + \frac{(f+F)'(f+F)''}{2r} + \frac{(f+F)''^2}{8} \right] , \quad (15)$$

$$R_{abcd}R^{abcd} = \frac{4(f+F-1)^2}{r^4} + \frac{4(f+F)'^2}{r^2} + (f+F)''^2 . \quad (16)$$

These expressions resemble those of the Schwarzschild case when $f = g = 1$ i.e., $\{R, R_{ab}R^{ab}, R_{abcd}R^{abcd}\} = \{0, 0, \frac{12rs^2}{r^6}\}$. Moreover, we illustrate three curvature

invariants as radial function in Fig. 3. It is clear that all curvature scalars diverge as $r \rightarrow 0$ and are finite for $r > 0$. This indicates that the spacetime metric (13) possesses an essential singularity, while the event horizon r_H is merely a coordinate singularity. In addition, we observe that the Ricci scalar is always negative which infers that the spacetime considered here is non-Ricci flat.

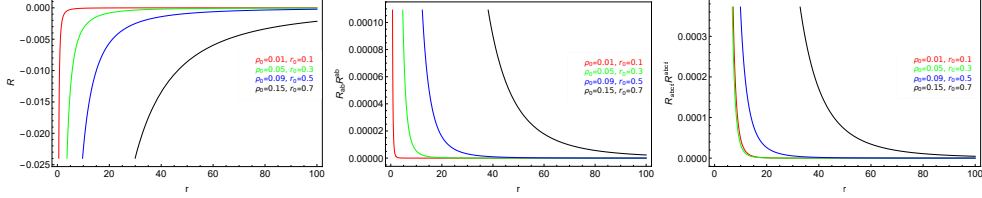


Fig. 3 Graphical demonstration of three curvature invariants Left: R , Middle: $R_{ab} R^{ab}$ and Right: $R_{abcd} R^{abcd}$.

To gain a deeper understanding of the spacetime background (1), we shall consider energy conditions. First, we obtain the energy momentum tensor $T_{\mu}^{\nu} = \text{diag}[-\rho_E, p_r, p, p]$ from the Einstein field equations (3)-(5)

$$\rho_E = -p_r = \frac{1}{8\pi r^2} - \frac{e^{4M_{DM}\left(\frac{1}{r} + \frac{1}{r_0}\right)}(r + 2M_{DM})}{8\pi r^3}, \quad (17)$$

$$p = \frac{M_{DM} e^{4M_{DM}\left(\frac{1}{r} + \frac{1}{r_0}\right)}}{16\pi r^4} \left[\frac{3rr_0 + 4M_{DM}(r + r_0)}{(r + r_0)} \right]. \quad (18)$$

With the presence of dark matter halo, we probe four energy conditions as a result of spacetime metric (13) i.e., null, weak, dominant, and strong energy conditions.

The null energy condition (NEC) states that for all null vectors n^a , the energy momentum tensor must satisfy

$$T_{ab} n^a n^b \geq 0. \quad (19)$$

This puts the following constraint on the energy density and pressure [28, 33]

$$\rho_E + p_j \geq 0, \quad (20)$$

where $j = 1, 2, 3$ and $p_1 = p_r, p_2 = p_3 = p$. From (17), it is obvious that $\rho_E + p_r = 0$. Hence, the NEC solely depends on $\rho_E + p \geq 0$. This reads explicitly

$$\frac{1}{8\pi r^2} + e^{4M_{DM}\left(\frac{1}{r} + \frac{1}{r_0}\right)} \left[\frac{M_{DM}^2}{4\pi r^4} - \frac{1}{8\pi r^2} - \frac{M_{DM}(4r + r_0)}{16\pi r^3(r + r_0)} \right] \geq 0. \quad (21)$$

The weak energy condition (WEC) implies that the total energy density as measured by any time-like observer (u^a) is always positive. Mathematically, this can be

written as

$$T_{ab}u^a u^b \geq 0. \quad (22)$$

It can be translated into the constraints on ρ_E , p_r and p as [28, 33]

$$\rho_E \geq 0, \quad \rho_E + p_j \geq 0. \quad (23)$$

This adds one additional constraint to the NEC. Therefore, if the WEC is satisfied, the NEC will simultaneously hold. However, the energy density, ρ_E (17), is never positive. This is because the only positive term is $\frac{1}{8\pi r^2}$ which will always be subjugated by $-\frac{e^{4M_{DM}}(\frac{1}{r} + \frac{1}{r_0})}{8\pi r^2}$. Thus, only the second condition of the WEC might possibly be satisfied.

The physical interpretation of the dominant energy condition (DEC) is that the local energy flux cannot propagate faster than the speed of light relative to any local future-directed observer [28]. Equivalently, this can be translated into

$$\rho_E - |p| \geq 0, \quad (24)$$

or

$$\frac{1}{8\pi r^2} - e^{4M_{DM}}\left(\frac{1}{r} + \frac{1}{r_0}\right) \left[\frac{M_{DM}^2}{4\pi r^4} + \frac{1}{8\pi r^2} + \frac{M_{DM}(4r + 7r_0)}{16\pi r^3(r + r_0)} \right] \geq 0. \quad (25)$$

It turns out that the DEC is never positive in the same manner as the ρ_E .

Lastly, the strong energy condition (SEC) states that [28]

$$\left(T_{ab} - \frac{1}{2}Tg_{ab} \right) n^a n^b \geq 0, \quad (26)$$

which yields

$$\rho_E + p_r + 2p \geq 0. \quad (27)$$

Hence, we obtain

$$\frac{e^{4M_{DM}}\left(\frac{1}{r} + \frac{1}{r_0}\right) M_{DM}}{2\pi r^3} \left[\frac{3r_0}{4(r + r_0)} + \frac{M_{DM}}{r} \right] \geq 0. \quad (28)$$

The expression on the left hand side is clearly positive for all r . Therefore, the SEC is generally satisfied.

Furthermore, asymptotic behavior of these energy conditions are as follow

$$\lim_{r \rightarrow 0} \{ (21), (23), (25), (28) \} = \pm\infty, \quad (29)$$

$$\lim_{r \rightarrow \infty} \{ (21), (23), (25), (28) \} = 0. \quad (30)$$

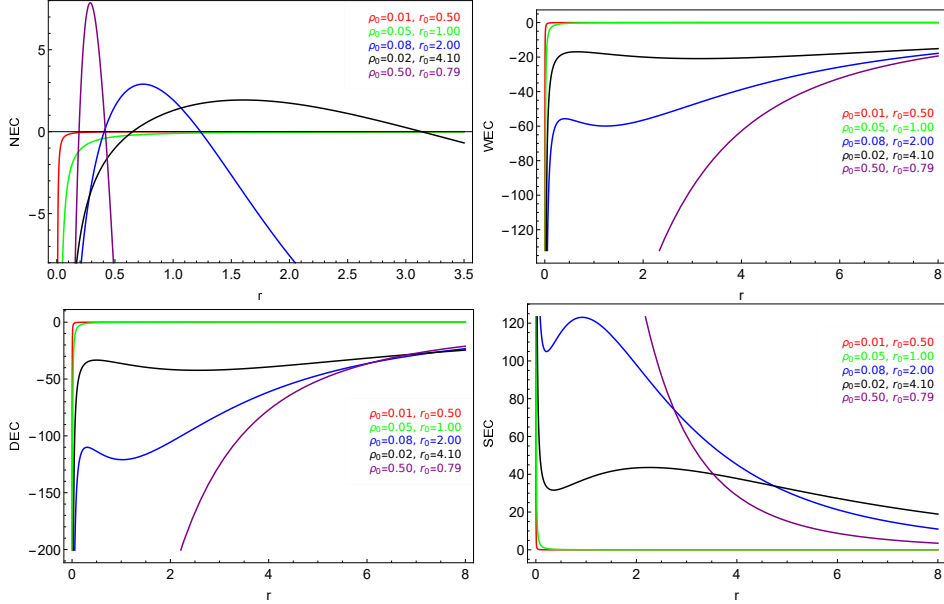


Fig. 4 Four energy conditions as radial function for various value of ρ_0 and r_0 . In the WEC panel, only $\rho_E \geq 0$ is shown.

To complete our analysis, we present how each energy condition (NEC, WEC, DEC and SEC) behave as a function of the radial coordinate for fixed value of ρ_0 and r_0 in Fig. 4. We provide a graphical analysis of the inequalities given by (21), (23) (only the first condition), (25) and (28). The positive regions in these figures illustrate the regions where the respective energy conditions are satisfied. It is observed that the NEC can be satisfied if the product between ρ_0 and r_0 is sufficiently large. In addition, we find that the positive regions in the NEC panel occur outside the event horizon. However, after reaching certain radii, the NEC is no longer satisfied. The WEC and DEC are, however, violated as discussed earlier. We remark that the second condition of the WEC is satisfied similarly to the NEC panel. Finally, we find that the SEC is satisfied for all r .

In the presented solution, the introduction of dark matter significantly modifies the stress-energy tensor, leading to an effective anisotropic fluid. In particular, the radial pressure p_r can become positive over a substantial region of spacetime. When combined with a sufficiently small energy density or strong pressure anisotropy, this behavior results in violations of the weak and dominant energy conditions. Physically, these violations originate from the smearing of the dark matter distribution over a characteristic length scale, a mechanism that is known to regularize the geometry at the expense of classical energy conditions. Such features are common in quantum-inspired and dark-matter-inspired black hole models, i.e., while they allow

for singularity-free configurations, they generically violate the WEC and/or DEC. Indeed, under physically reasonable assumptions on the mass function, all known regular and rotating black hole solutions violate the weak energy condition somewhere in the spacetime [34–40]. Moreover, recent studies have also reported violations of the weak and dominant energy conditions for static black holes immersed in Hernquist dark matter halos [41, 42].

3 Black Hole Thermodynamics

In this section, we investigate the thermodynamics of a Schwarzschild black hole immersed in the Dehnen $(1, 4, \frac{3}{2})$ dark matter profile. We begin by considering the position of the horizon r_H , which is obtained from,

$$g_{tt}(r_H) = 0 \rightarrow e^{\frac{32}{3}\pi\rho_0 r_0^2 \left(1 + \frac{r_0}{r_H}\right)^{-1/2}} - \frac{2M}{r_H} = 0, \quad (31)$$

or equivalently,

$$M = \frac{r_H}{2} e^{\frac{32}{3}\pi\rho_0 r_0^2 \left(1 + \frac{r_0}{r_H}\right)^{-1/2}}. \quad (32)$$

As one can see, in the absence of dark matter $\rho_0 = 0$. The above relation reduces to the Schwarzschild radius ($r_H = r_s = 2M$). In black hole thermodynamics, the equivalent enthalpy of classical thermodynamics is exactly the mass M as given by (32) [43, 44].

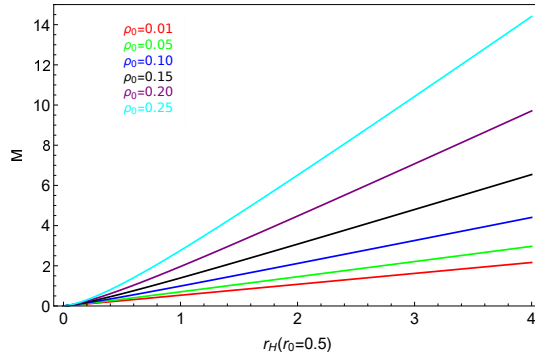


Fig. 5 The mass function plotted against r_H for different core density ρ_0 and fixed $r_0 = 0.5$.

We illustrate the mass of black hole as a function of the event horizon r_H for various central density ρ_0 and fixed core radius $r_0 = 0.5$ in Fig. 5. As expected, the mass increases with r_H . The more central density, the higher the rate of increasing. The mass function differs significantly as r_H gets larger. A similar trend is also observed for the other value of r_0 . However, in smaller r_0 , the difference of each curve becomes less significant.

The surface gravity of the horizon κ defines the Hawking temperature as follows, $T = \frac{\kappa}{2\pi} = \frac{f' + F'}{4\pi}|_{r=r_H}$. The temperature reads

$$T = e^{\frac{32}{3}\pi\rho_0 r_0^2 \left(1 + \frac{r_0}{r_H}\right)^{-1/2}} \left[\frac{1}{4\pi r_H} + \frac{4}{3} \frac{\rho_0 r_0^3}{\sqrt{r_H(r_0 + r_H)^3}} \right]. \quad (33)$$

Note that if ρ_0 is set to zero, we recover the Schwarzschild black hole's Hawking temperature $T = \frac{1}{8\pi M}$. Moreover, at large r_H , the temperature decreases as $\frac{1}{r_H}$ and asymptotically approaches zero. Fig. 6 shows the black hole's temperature T with respect to r_H for various combinations of $\{\rho_0, r_0\}$. The left (right) panel depicts the behavior of T with fixed $r_0 = 2$ ($\rho_0 = 0.01$). In the Schwarzschild case ($\rho_0 = 0$, red curve), the temperature decreases monotonically with r_H . Thus, the slope is always negative. For sufficiently large dark matter density ρ_0 , the temperature profiles have interesting character. At first, the temperature develops to a minimum at a certain r_H . As r_H increases, the temperature reaches its maximum before decreasing with r_H . This clearly indicates at least three branches of black hole, i.e., the small black hole with negative $\frac{\partial T}{\partial r_H}$, the intermediate black hole with positive $\frac{\partial T}{\partial r_H}$ and sufficiently large black hole with negative $\frac{\partial T}{\partial r_H}$. For small ρ_0 , the temperature profile only decreases with r_H .

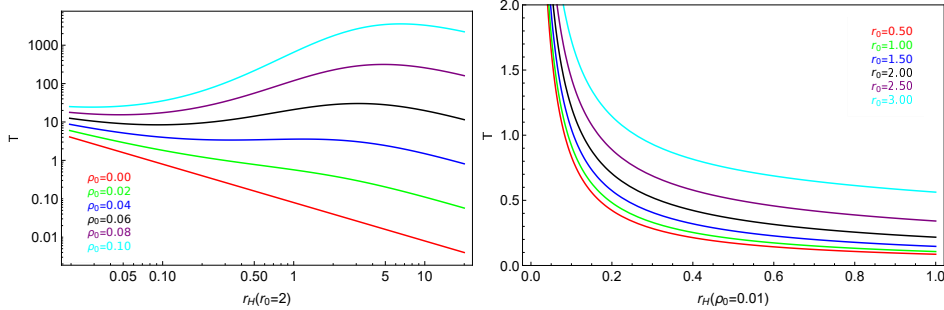


Fig. 6 Profile of temperature as function of r_H for various $\{\rho_0, r_0\}$. The left panel is displayed in a log-log scales.

The black hole's entropy can be computed directly from [25]

$$S = \int \frac{1}{T} \frac{dM}{dr_H} dr_H = \pi r_H^2 = \frac{A}{4}, \quad (34)$$

where the surface area of the black hole is $A = 4\pi r_H^2$. This agrees with the Bekenstein black hole's entropy formula [45] where the entropy of the black hole is proportional to the black hole's surface area. In addition, the dark matter halo has no contribution to the entropy of the event horizon.

To investigate the thermal stability of a black hole as a thermodynamic system, the heat capacity must be calculated. A positive heat capacity indicates a stable

thermodynamic system, while a negative heat capacity indicates instability [46, 47]. Positive heat capacity means that the black hole-dark matter system requires energy to increase its temperature, whereas negative heat capacity indicates that the system cools down as heat is injected. In other words, black hole with negative heat capacity gets hotter as it radiates more heat.

The specific heat capacity is obtained as follows,

$$C_H = \frac{\partial M}{\partial T} = \frac{\frac{\partial M}{\partial r_H}}{\frac{\partial T}{\partial r_H}} = -\frac{6\pi r_H^2(r_0 + r_H) \left\{ 3(r_0 + r_H)^2 + 16\pi\rho_0 r_0^3 \sqrt{r_H(r_0 + r_H)} \right\}}{9(r_0 + r_H)^3 - 256\pi^2\rho_0^2 r_0^6 r_H - 24\pi\rho_0 r_0^3(r_0 - 2r_H) \sqrt{r_H(r_0 + r_H)}}. \quad (35)$$

The heat capacity simply reduces to those of the Schwarzschild black hole $C_H = -2\pi r_H^2$ as $\rho_0 \rightarrow 0$ [48]. The black hole's heat capacity C_H in relation to r_H for different combinations of $\{\rho_0, r_0\}$ is displayed in Fig. 7. The behavior of T with fixed $r_0 = 2$ ($\rho_0 = 0.1$) is seen in the left (right) panel. The behavior of the heat capacity C_H is directly related to the slope of the temperature $T(r_H)$ function.

It is important to note that the C_H curves break at the extrema of $T(r_H)$, i.e., when $\frac{\partial T}{\partial r_H} = 0$. It is clear that the stable (unstable) branch with $C_H > 0(< 0)$ corresponds to the portion of the temperature function with a positive (negative) slope. Black hole + dark matter configurations without an inflection point, or with a tiny ρ_0 , do not have a thermodynamically stable branch. In the Schwarzschild limit, temperature decreases monotonically with r_H , resulting in a negative heat capacity throughout the domain, highlighting the instability of asymptotically flat black holes in the classical ensemble [49].

When dark matter is added, the structure of $T(r_H)$ changes and regions with a positive slope appear, corresponding to domains with a positive heat capacity, indicating a thermodynamically stable branch. Interestingly, when $\rho_0 = 0.02$ (left panel) and $r_0 = 1.0$, the heat capacity profile remains similar to that of the Schwarzschild case, indicating that these configurations are thermodynamically unstable. At sufficiently large ρ_0, r_0 , the heat capacity structure becomes more non-trivial. It is observed that for a fixed $\{\rho_0, r_0\}$, there are two transition points where C_H diverges. The divergence of heat capacity suggests an existence of second-order phase transition [50–52]. The radius at which the transitions occur can be obtained by setting the denominator of (35) to zero. For instance, for $\rho_0 = 0.04$ and $r_0 = 2$, we find that the transitions locate at $r_H = 0.33$ and $r_H = 1.17$. Although it cannot be seen easily from the plots in the left panel, we also find two second-order phase transitions for $\rho_0 = 0.06, 0.08, 0.10$ (black, purple, cyan). In addition, as $\rho_0(r_0)$ gets larger, the two transition points also grows apart.

The transition from the unstable to stable at smaller r_H then shift to the unstable again at large r_H implies that sufficiently small and large black holes with the Dehnen dark matter profile are thermodynamically unstable. Transitions from thermodynamically unstable to stable regimes and vice versa, occur at the temperature function's extreme points. Increasing the core dark matter density broadens the range

of r_H for which the heat capacity is positive, extending the stable phase of the black hole-dark matter system. In contrast to Schwarzschild black hole case, this shows how the surrounding Dehnen $(1, 4, \frac{3}{2})$ dark matter halo can act as a stabilizing medium.

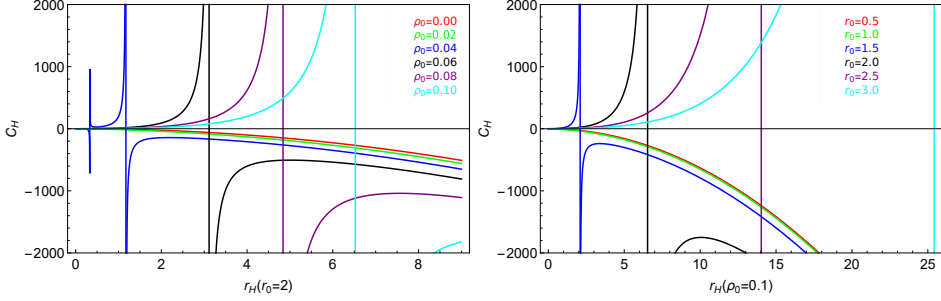


Fig. 7 Profile of C_H as function of r_H for various $\{\rho_0, r_0\}$. The case $\rho_0 = 0$ in the left panel indicates heat capacity of the Schwarzschild black hole.

To assess the overall stability of the black hole with dark matter system, we study the Gibbs free energy G in our model. A positive G indicates instability in the thermodynamic system, whereas a negative value shows stability. The Gibbs free energy is computed as,

$$G = M - TS, \\ = e^{\frac{32}{3}\pi\rho_0 r_0^2 \left(1 + \frac{r_0}{r_H}\right)^{-1/2}} r_H \left[\frac{1}{4} - \frac{4}{3}\pi\rho_0 r_0^3 \sqrt{\frac{r_H}{(r_H + r_0)^3}} \right]. \quad (36)$$

Figure 8 shows the black hole's Gibbs free energy G as a function of r_H for various combinations of $\{\rho_0, r_0\}$. The top (lower) graph shows how G behaves with fixed $r_0 = 2$ ($\rho_0 = 0.04$). Our findings indicate that the negative region of the Gibbs free energy increases with higher core density and halo radius. Both graphs demonstrate that the presence of a dark matter halo, in general, increases the black hole's global stability. Later, the Gibbs free energy turns positive at greater r_H indicating that black holes are thermodynamically unstable at large r_H .

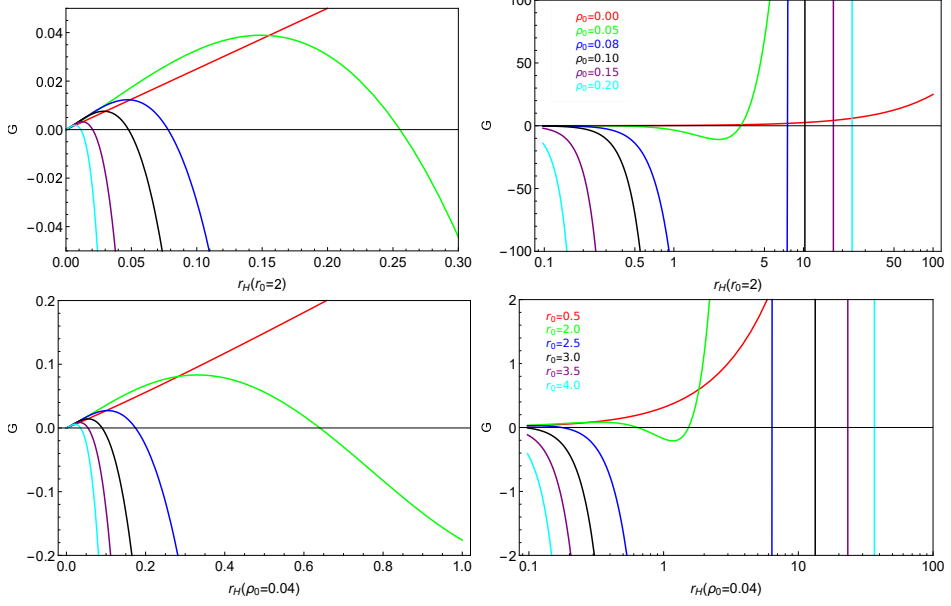


Fig. 8 Profile of G as function of r_H for various $\{\rho_0, r_0\}$. The left panel depicts the behavior of G at small r_H while the right panel illustrates the behavior of G at a broader range of r_H .

Figure 9 shows the entropy, heat capacity and Gibbs free energy as functions of temperature with fixed $r_0 = 2$. In these plots, the arrows mark direction of increasing horizon radius r_H . The smaller black holes (small r_H) corresponding to lower entropies and higher temperatures, while larger black holes (large r_H) occupy the opposite end. Importantly, the entropy remains continuous across the entire temperature range. There is an inflection point at critical temperature for each curve with large enough ρ_0 where $\frac{dS}{dr_H}$ changes sign.

The heat capacity $C_H(T)$, however, displays a remarkably different behavior. For small black holes, the heat capacity is negative and as r_H increases, the system encounters divergences in $C_H(T)$, marking second-order phase transitions from small to large black hole. For large black hole regime, the heat capacity is positive, indicating the existence of locally stable black hole branches supported by the halo. More investigation has revealed that for $\rho_0 = 0.02$ case, the heat capacity remains negative. In contrast, for the $\rho_0 > 0.02$ cases, we find that as temperature increases another second-order phase transition occurs which marks the transition from positive heat capacity to negative one.

The Gibbs free energy $G(T)$ of small black holes (at high temperatures) exhibit positive free energy and are globally unstable, while large black holes with positive C_H show negative $G(T)$, identifying them as thermodynamically favored states. Moreover, at the critical points where

$$\frac{\partial G(T)}{\partial T} = \frac{\partial^2 G(T)}{\partial T^2} = 0. \quad (37)$$

We observe the following distinct properties: The Gibbs function $G(T)$ and its slope $\frac{\partial G(T)}{\partial T}$ are continuous, whereas $\frac{\partial^2 G(T)}{\partial T^2}$ is not. According to Ehrenfest's classification, it clearly represents a second-order phase transition. Also note that a phase transition occurs if ρ_0 is sufficiently large.

Taken together, Fig. 9 demonstrate that the Dehnen $(1, 4, \frac{3}{2})$ dark matter halo introduces a stable thermodynamically phase of static spherically symmetric black hole, enriching the phase structure and highlighting how dark matter can act as a thermodynamically stabilizing medium.

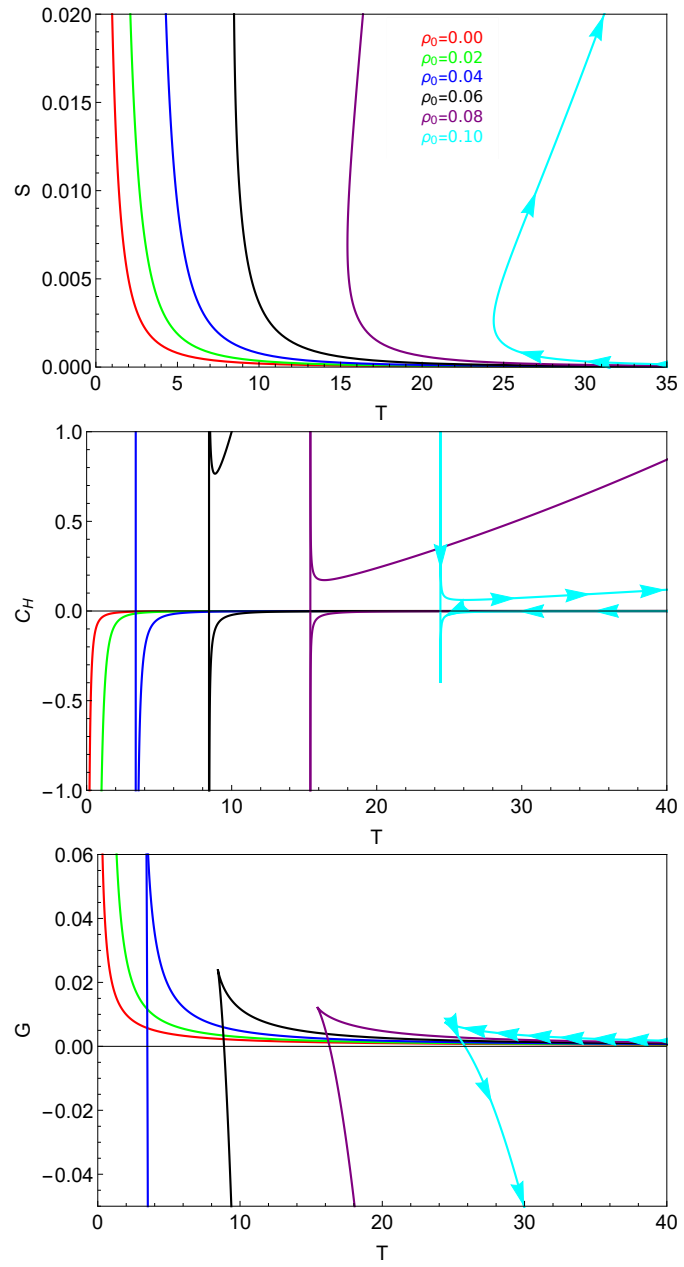


Fig. 9 Profile of $S(T)$, $C_H(T)$ and $G(T)$ for fixed $r_0 = 2$ and various ρ_0 . The arrow indicates the direction of increasing r_H .

4 Null Geodesic and Black Hole's Shadow

Null geodesics are the paths followed by light in curved spacetime. Around a black hole, these trajectories determine which photons escape to infinity and which are captured. The boundary between these two outcomes forms the photon sphere and when projected onto the observer's sky, it defines the black hole's shadow—a dark silhouette surrounded by a bright emission ring [53].

Now, let us consider photon trajectory around the Schwarzschild black hole immersed in the Dehnen $(1, 4, \frac{3}{2})$ dark matter halo. We start by writing the Lagrangian of a massless particle,

$$\mathcal{L}(x, \dot{x}) = \frac{1}{2} g_{ab} \dot{x}^a \dot{x}^b = 0, \quad (38)$$

where g_{ab} is the metric tensor components given by (13) and $\dot{x}^a = dx^a(\lambda)/d\lambda$ where λ is the curve parameter. Substituting the metric tensor components into the Lagrangian, it is straightforward to obtain the following expression,

$$\mathcal{L}(r, \theta, \dot{t}, \dot{r}, \dot{\theta}, \dot{\phi}) = \frac{1}{2} \left[-h(r) \dot{t}^2 + \frac{\dot{r}^2}{h(r)} + r^2 \dot{\theta}^2 + r^2 \sin^2 \theta \dot{\phi}^2 \right], \quad (39)$$

where $h(r)$ can be found in (13). There are two constants of motion, i.e., in the temporal and the azimuthal directions. This is because the Lagrangian (39) is not an explicit function of t and ϕ . These constants are

$$p_t = \frac{\partial \mathcal{L}}{\partial \dot{t}} = -h(r) \dot{t} = -E, \quad (40)$$

$$p_\phi = \frac{\partial \mathcal{L}}{\partial \dot{\phi}} = r^2 \dot{\phi} \sin^2 \theta = L, \quad (41)$$

where E and L denote the photon's energy and angular momentum, respectively.

In the equatorial plane $\theta = \frac{\pi}{2}$, the Lagrangian (39) is further simplified,

$$\begin{aligned} \mathcal{L}(r, \dot{t}, \dot{r}, \dot{\phi}) &= \frac{1}{2} \left[-h(r) \dot{t}^2 + \frac{\dot{r}^2}{h(r)} + r^2 \dot{\phi}^2 \right] \\ &= \frac{1}{2} \left[-\frac{E^2}{h(r)} + \frac{\dot{r}^2}{h(r)} + \frac{L^2}{r^2} \right] = 0. \end{aligned} \quad (42)$$

This implies the following radial equation

$$\dot{r}^2 + V_{eff} = \frac{1}{b^2}, \quad (43)$$

where we have defined $\bar{\lambda} \equiv \lambda L$ and the impact parameter $b^2 = L^2/E^2$. The first and second terms on the left-hand side represent the radial kinetic energy and effective potential V_{eff} . Note that, from this point onward $\dot{r} = dr/d\bar{\lambda}$. The explicit form of the

effective potential is

$$V_{eff} = \frac{h}{r^2} = \frac{1}{r^2} \left[e^{\frac{32}{3}\pi\rho_0 r_0^2 (1+\frac{r_0}{r})^{-\frac{1}{2}}} - \frac{r_s}{r} \right]. \quad (44)$$

A maximum of the effective potential signifies the location of photon circular orbits. These circular orbits are, in fact, unstable. This is because a slight perturbation may cause the photon moving away from the peak. The radius of the photon sphere r_{ph} can be computed from the following conditions

$$\frac{d}{dr} V_{eff}(r_{ph}) = 0, \quad V_{eff}(r_{ph}) = \frac{1}{b_c^2}, \quad (45)$$

where b_c is the critical impact parameter. The first condition yields

$$\left(\frac{h'}{r^2} - \frac{2h}{r^3} \right) \Big|_{r=r_{ph}} = 0. \quad (46)$$

Since at the event horizon $r = r_H$, the second term above vanishes, while the first term is generally non-zero. This implies that $r_H \neq r_{ph}$. Unfortunately, the photon sphere radius cannot be expressed explicitly due to the complication in (46). However, it is possible to show that for a small ρ_0 , The radius of the photon sphere can be determined from

$$0 = \frac{6 - 2r_{ph}}{r_{ph}^4} - \frac{16\pi r_0^2}{3r_{ph}^4} (4r_{ph} + 3r_0) \left(\frac{r_{ph}}{r_{ph} + r_0} \right)^{3/2} \rho_0 + \mathcal{O}(\rho_0)^2. \quad (47)$$

At the zero order, the photon sphere radius simply reduces to those of the Schwarzschild case $r = r_{ph} = 3$. On the other hand, the critical impact parameter can be obtained anallytically

$$b_c = \pm \frac{r_{ph}^{3/2}}{\sqrt{r_{ph} e^{32\pi r_0^2 \rho_0 \left(\frac{r_{ph}}{r_{ph} + r_0} \right)^{1/2}} - 2}}. \quad (48)$$

In the Schwarzschild limit ($\rho_0 = 0, r_{ph} = 3$), the critical impact parameter above becomes $b_c = 3\sqrt{3}$.

At two asymptotic region, the effective potential and its derivative take the form

$$\begin{aligned} V_{eff}(r \rightarrow 0) &= -\frac{2}{r^3} + \mathcal{O}(1/r^2), & V'_{eff}(r \rightarrow 0) &= \frac{6}{r^4} + \mathcal{O}(1/r^3), \\ V_{eff}(r \rightarrow \infty) &= \frac{e^{32\pi r_0^2 \rho_0 / 3}}{r^2} + \mathcal{O}(1/r^3), & V'_{eff}(r \rightarrow \infty) &= -2\frac{e^{32\pi r_0^2 \rho_0 / 3}}{r^3} + \mathcal{O}(1/r^4). \end{aligned} \quad (49)$$

Given that $V_{eff}(r)$ starts negative with an increasing slope as $r \rightarrow 0$ and becomes positive with a decreasing slope as $r \rightarrow \infty$ continuity implies the existence of at least one point in between where the derivative of $V_{eff}(r)$ vanishes, i.e., a maximum. The photon sphere is guaranteed if the maximum occurs outside the event horizon.

Figure 10 shows a graph of the effective potential behavior for different black hole parameters combinations with respect to r . It is observed that as ρ_0 and r_0 increase, the maximum height of the effective potential (V_{max}) increases. This implies that the critical impact parameter b_c decreases with ρ_0 and r_0 . Moreover, the unstable photon circular orbit (r_{ph}) becomes smaller while ρ_0 and r_0 get larger.

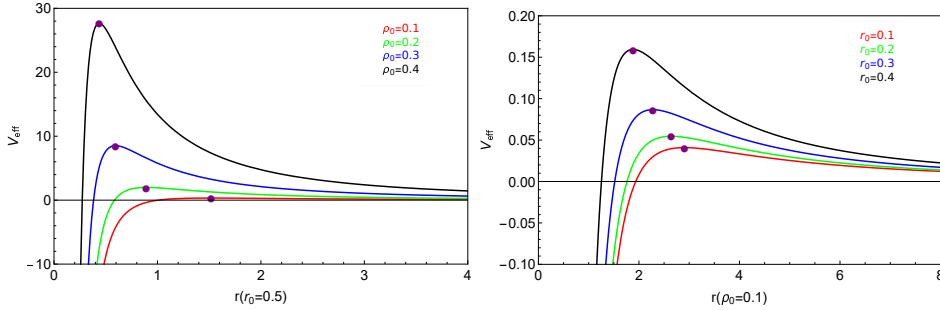


Fig. 10 Profile of V_{eff} for selected combinations of black hole parameter. The purple dots mark the location of $V_{eff}(r_{ph}) = V_{max}$.

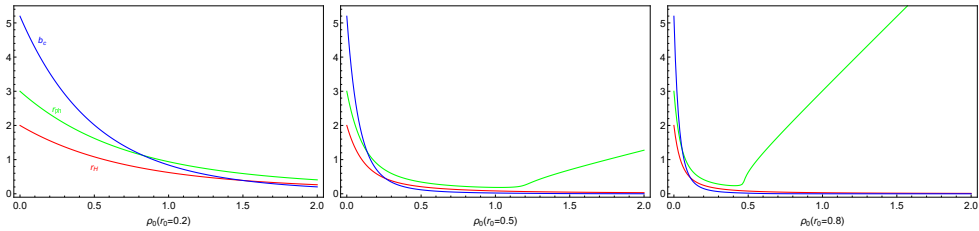


Fig. 11 The behavior of r_H , r_{ph} and b_c as function of ρ_0 for three specified values of r_0 .

Additionally, black hole's event horizon (r_H), photon sphere radius (r_{ph}) and critical impact parameter (b_c) are plotted against halo's central density ρ_0 as illustrated in Fig. 11. First of all, at $\rho_0 = 0$, these parameters resemble those of the Schwarzschild black hole i.e., $r_H = 2$, $r_{ph} = 3$, $b_c = 3\sqrt{3}$. At small $r_0 = 0.2$, we observe a clear monotonic decreasing behavior of these parameters confirming our earlier discussion. As core's radius gets larger, we notice that the photon sphere radius instead of decreasing with ρ_0 but increasing after a certain value of ρ_0 . Moreover, at larger r_0 , the increasing of r_{ph} against ρ_0 occurs at smaller ρ_0 . The plot also depicts that the event horizon and photon sphere never coincide.

One can consider the case $\rho_0 \gg 1$ in the region with sufficiently large r_{ph} compared to r . Under this condition, (46) can be approximated as

$$-2 + \frac{16\pi r_0^3 \rho_0}{r_{ph}} = 0 \quad \Rightarrow \quad r_{ph} = 8\pi r_0^3 \rho_0, \quad (50)$$

which shows that r_{ph} scales linearly with ρ_0 with slope proportional to r_0^3 .

4.1 Black Hole's Shadow

The propagation of photons in the strong gravitational field of a black hole exhibits a rich variety of behaviors that underlie key observational phenomena. Photon trajectories can be categorized into three distinct classes: those captured by the event horizon, those temporarily stay in unstable circular orbits and those deflected to infinity after partial revolutions. Only the latter two classes are accessible to a distant observer, with the unstable circular orbit—known as the photon sphere—defining the critical boundary between captured and escaped. The properties of this orbit govern the structure of black hole shadows. To a distant observers, black holes are illuminated by a bright photon ring. The inner edge of it defines black hole's shadow.

Additionally, the circular orbit of photons is fundamentally unstable. Small perturbations determine whether the object spirals toward or escapes the black hole. As a result, backward ray tracing of these departing photons from the photon sphere will travel through the intervening space, influenced by dark matter. These photons originate in the photon sphere and travel reaching the observer at the critical impact parameter. Thus, we can observe how the photon sphere and impact parameter connect to the shadow's perceived angular radius and radius.

Using (45), we can write the critical impact parameter b_c as,

$$b_c^{-1} = \sqrt{\frac{h(r_{ph})}{r_{ph}^2}}. \quad (51)$$

An observer at spatial infinity can measure the shadow radius radius R_s as [54],

$$R_s = b_c \sqrt{h(r \rightarrow \infty)} \approx \sqrt{\frac{r_{ph}^2}{h(r_{ph})}} e^{\frac{16}{3}\pi\rho_0 r_0^2}. \quad (52)$$

In asymptotically flat spacetimes such as the Schwarzschild or Reissner-Nordström black holes, the redshift function satisfies $h(r \rightarrow \infty) \rightarrow 1$. Consequently, the shadow radius measured by a distant observer coincides with the critical impact parameter, $R_s = b_c$. In the present case, the Dehnen $(1, 4, \frac{3}{2})$ halo alters the asymptotic structure of the spacetime, giving $h(r \rightarrow \infty) = e^{\frac{16}{3}\pi\rho_0 r_0^2}$ which is generally non-unity. The metric therefore approaches a *conformally flat* rather than a truly asymptotically flat geometry. As a result, the propagation of photons from the photon sphere to infinity results in an additional constant redshift factor, as given in (52). Interestingly, this distinction is due to the effect of the surrounding dark-matter halo on optical geometry.

For special case with $\rho_0 r_0^3 \ll 1$, we can perform series expansion to (47) and obtain the radius of photon sphere,

$$r_{ph} \approx \frac{3(3r_s + 16\pi\rho_0 r_0^3)}{2(3 + 32\pi\rho_0 r_0^2)}, \quad (53)$$

yielding,

$$R_s \approx \frac{\sqrt{3}}{2} \left[3r_s + 16\pi\rho_0 r_0^3 \left(1 - 2\frac{r_s}{r_0} \right) \right], \quad (54)$$

where the expression $R_s = \frac{3\sqrt{3}}{2}r_s$ is recovered for the case without dark matter, which is obtained in [55].

Figure 12 depicts shadow casted by black holes as seen from remote observer. The upper left panel displays the shadow radius R_s against halo's central density ρ_0 for three distinct value of r_0 . At small r_0 , R_s decreases monotonically with ρ_0 . As r_0 increases, we observe that the shadow radius initially decreases and later increases with ρ_0 . This implies that at each fixed r_0 , the radius takes the smallest value at certain value of ρ_0 . Our numerical investigation reveals that the smallest shadow radii for $r_0 = 0.2, 0.5, 0.8$ cases occur at $\rho_0 = 4.05, 0.54$ and 0.19 respectively.

Moreover, we display shadow radius for various configurations of $\{\rho_0, r_0\}$. in the upper right, lower left and right panel (for $r_0 = 0.2, 0.5, 0.8$ respectively). The red circles in each panel present the shadow radius of the Schwarzschild black hole ($\rho_0 = 0$), $R_s = 3\sqrt{3} = 5.19615$. It is clear that as ρ_0 increases, the shadow radius becomes smaller for $r_0 = 0.2$. At larger r_0 , the shadow radius behavior turns out to be more complicated. At first, the radius decreases with ρ_0 and it reaches the smallest size at $\rho_0 = 0.5$ (0.05) for the lower left (right) panel. After that the radius is larger as ρ_0 increases.

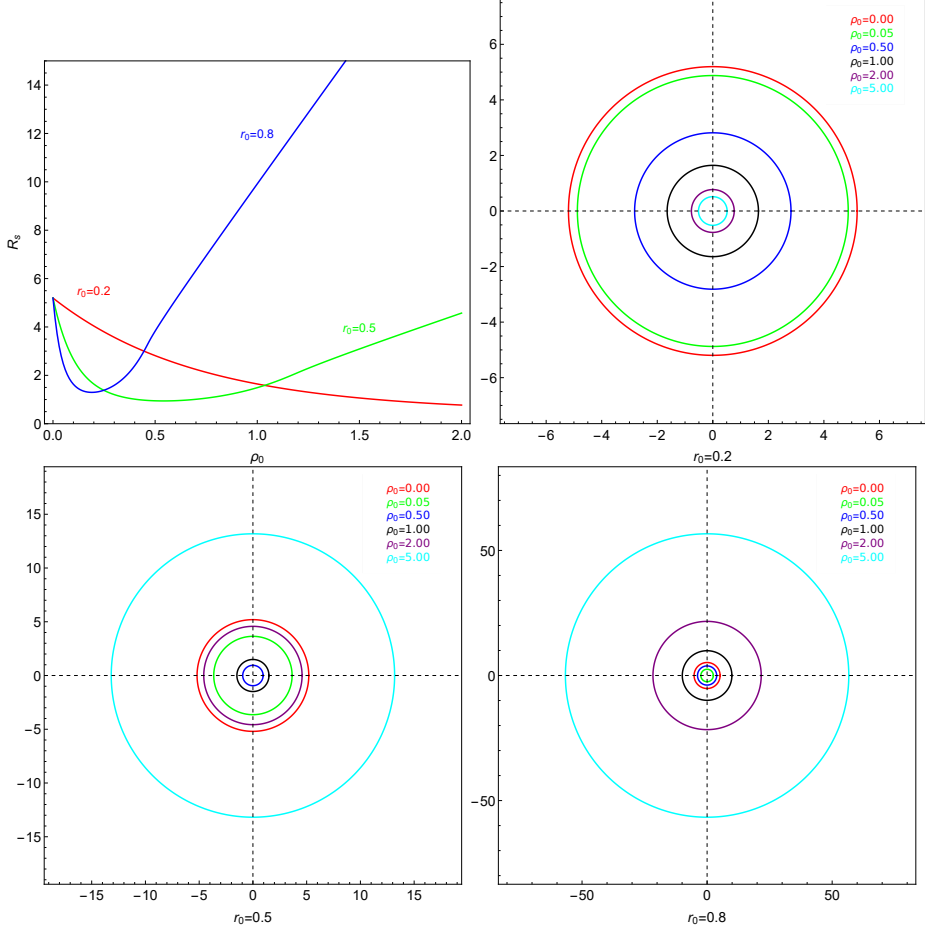


Fig. 12 Upper left: Shadow radius R_s as a function of ρ_0 for various $r_0 = 0.2, 0.5, 0.8$. Upper right and lower panels: Shadow casts as observed by distance observers. In these figures, we set $r_s = 2$.

By using observational data of $M87^*$ from the event horizon telescope (EHT) collaboration [2], the physical charges of black hole are constrained by using black hole shadow's radius [56]. It is found that the shadow size of $M87^*$ must lie within the range

$$4.31M_{BH} \leq R_s \leq 6.08M_{BH}. \quad (55)$$

For $SgrA^*$, the bounds are

$$4.5M_{BH} \leq R_s \leq 5.5M_{BH}, \quad (56)$$

$$4.3M_{BH} \leq R_s \leq 5.3M_{BH}, \quad (57)$$

from the Keck Observatory and the Very Large Telescope Interferometer, respectively [57]. In Fig. 13, we display shadow radius R_s as a function of ρ_0 together with the constraints from the $M87^*$ and $SgrA^*$. In these figures, we fix $r_0 = 0.2, 0.5$ and 0.8 which are represented by red, blue and purple dashed lines. The gray regions denote the area where black hole's shadow radii are inconsistent with constraints from the $M87^*$ and $SgrA^*$. There are, in general, two intervals of ρ_0 that makes R_s of the Dehnen-black hole are compatible with the observation data depending on the chosen r_0 .

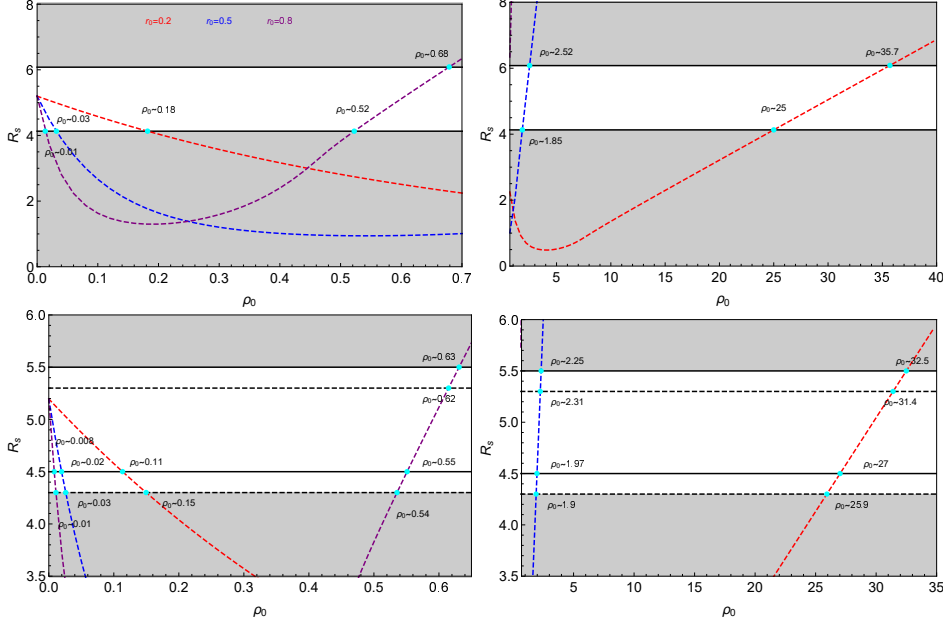


Fig. 13 Constraint on shadow Radius R_s expresses in term of ρ_0 compared with $M87^*$ data (top) and $SgrA^*$ data (bottom). There are three distinct profiles of $r_0 = 0.2, 0.5$ and $r_0 = 0.8$ illustrated by red, blue and purple curved. The cyan dots mark the value ρ_0 at the lower and upper bounds of R_s . The left panel represents configuration with small ρ_0 while the right panel is the same configuration but with larger ρ_0 . Top: The region where the shadow radius is inconsistent with $M87^*$ data is denoted by gray color. Bottom: The allowed region is denoted by white color where the bounds from Keck (VLTI) are marked with black solid (dashed) horizontal lines.

Finally, it is worth noting that while astrophysical black holes like $SgrA^*$ and $M87^*$ do rotate, using the constraints from these sources to a non-rotating black hole may lead to unrealistic conclusions. However, it has been demonstrated in [54, 58] that these sources can nevertheless effectively constrain the parameters of non-rotating spacetime geometry.

4.2 Weak Gravitational Lensing

Now we examine the weak deflection angle of particles in a static black hole immersed in a Dehnen-type $(1, 4, \frac{3}{2})$ dark matter. Weak gravitational lensing (WGL) is a powerful observational technique that enables the measurement of mass distributions in the universe, including galaxies, clusters and large-scale structures. By analyzing the subtle distortions imprinted on the images of background sources, WGL provides a direct and unbiased probe of both luminous and dark matter, making it an essential tool for cosmology and astrophysics [18, 59]. To calculate the weak-field deflection angle, we use the Gauss-Bonnet theorem as applied to the optical metric and Gibbons-Werner method to calculate the weak deflection angle [60, 61].

The deflection angle α is calculated from the following integral [62],

$$\alpha = \int_{\phi=0}^{\pi} \int_{r=\frac{b}{\sin \phi}}^{\infty} K \sqrt{g_{opt}} dr d\phi, \quad (58)$$

where K and g_{opt} are the Gaussian (3D) curvature and the determinant of the following optical metric,

$$dt^2 = \frac{dr^2}{h^2(r)} + \frac{r^2 d\phi^2}{h(r)}, \quad (59)$$

yielding,

$$g_{opt} = \frac{r^2}{h^3(r)}, \quad (60)$$

and,

$$K = \frac{1}{2} \left[h(r) \frac{d^2 h(r)}{dr^2} - \frac{1}{2} \left(\frac{dh(r)}{dr} \right)^2 \right]. \quad (61)$$

Using (13), we can write the integrand explicitly as a series up to $O(\rho_0 r_0^3)$ as follows,

$$K \sqrt{g_{opt}} \approx \frac{r_s}{r^2} - \frac{16\pi\rho_0 r_s r_0^2}{3r^2} + \frac{8\pi\rho_0 r_0^3}{r^3} \left(\frac{2r}{3} + r_s \right). \quad (62)$$

This leads to

$$\alpha \approx \frac{2}{3b} \left[(3 - 16\pi\rho_0 r_0^2) r_s + \rho_0 \pi r_0^3 (16 + 3\pi b^{-1} r_s) \right]. \quad (63)$$

Note that if $\rho_0 = r_0 = 0$, we obtain $\alpha = 2b^{-1}r_s$ which is the deflection angle of an isolated Schwarzschild black hole [61]. From (63), the positivity of deflection angle is guaranteed for $0 < \rho_0 < \frac{3}{16\pi r_0^2}$. Hence, this yields an upper bound of ρ_0 when r_0 is fixed. Otherwise, the positive deflection angle depends entirely on the mixing of b, ρ_0, r_0 . On the other hand, it is possible to obtain $\alpha < 0$ once the following conditions are met simultaneously

$$\rho_0 > \frac{3}{8\pi r_0 (2 - r_0)}, \quad b > \frac{3\rho_0 \pi^2 r_0^3}{8\pi (2 - r_0) \rho_0 r_0^2 - 3}, \quad 0 < r_0 < 2. \quad (64)$$

A negative deflection angle implies that light rays are bent away from the black hole rather than toward it. This behavior can be interpreted as an effective repulsive

gravitational influence. Similar repulsive effects have been reported in several previous studies (see [63–66] and references therein). In this case, the sign convention for the deflection angle means that counter-clockwise deviations are taken as positive, while clockwise deviations are negative, causing the light rays to miss the intended location of the receiver [64, 65].

Figure 14 illustrates the deflection angle for several r_0, ρ_0 values. This plot shows the gravitational deflection angle as a function of the impact parameter for black holes surrounded by Dehnen $(1, 4, \frac{3}{2})$ dark matter profile with black hole mass $M = 1$. The results show that for low impact parameters $b \rightarrow 0$, the deflection angle increases significantly, indicating a strong gravitational lensing effect as one moves closer to the black hole. As the impact parameter grows, the deflection angle falls and approaches zero, which is expected. Based on the inequalities (64), we choose the parameters such that (64) are satisfied to demonstrate negative deflection angle as a blue curve. In the right panel, we display deflection angle against impact parameter where the value of r_0 and ρ_0 agree with the bounds of Shadow radius discussed in the aforementioned subsection. Interestingly, even when the constraints from $M87^*$ and $SrgA^*$ are respected, the repulsive deflection angle remains visible.

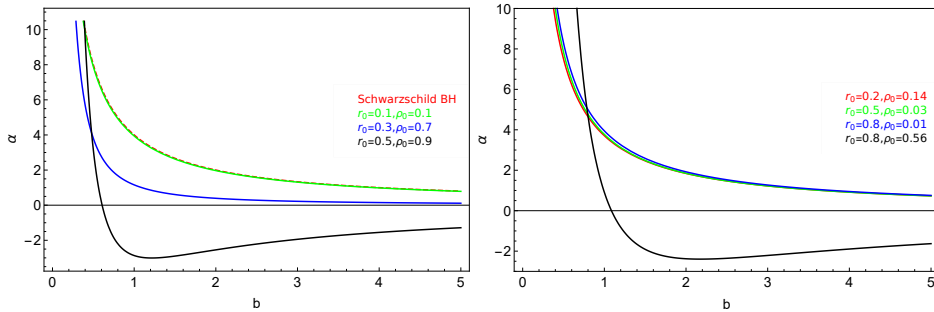


Fig. 14 Profile of deflection angle α as a function of impact parameter b for various r_0 and ρ_0 with fixed $r_s = 2$. Right: r_0 and ρ_0 are chosen to be consistent with bounds from $M87^*$ and $SrgA^*$.

5 Lyapunov Exponent

In this section, we investigate the Lyapunov exponent associated with the unstable circular orbits of test particles around the black hole embedded in the Dehnen dark matter halo. The Lyapunov exponent quantifies the rate of exponential divergence between neighboring trajectories and thus provides a direct measure of the orbital instability in the spacetime. Since the presence of the halo alters the geometry and the shape of the effective potential, the stability properties of circular orbits are expected to differ from those in the pure Schwarzschild case.

To analyze the instability of null geodesics, let us first recall the radial null geodesics from (42)

$$\dot{r}^2 = V_r(r) = E^2 - \frac{h(r)L^2}{r^2}. \quad (65)$$

Now let us consider the Euler-Lagrange equation

$$\frac{dp_q}{d\lambda} = \frac{d}{d\lambda} \left(\frac{\partial \mathcal{L}}{\partial \dot{q}} \right) = \frac{\partial \mathcal{L}}{\partial q}, \quad (66)$$

where p_q is generalized momenta. By linearizing the equation of motion above around circular orbit of constant r , one may define an infinitesimal evolutionary matrix [67]

$$K_{ij} = \begin{pmatrix} 0 & K_1 \\ K_2 & 0 \end{pmatrix}, \quad (67)$$

where

$$K_1 = \frac{d}{dr} \left(\dot{t}^{-1} \frac{\partial \mathcal{L}}{\partial r} \right), \quad (68)$$

$$K_2 = \frac{1}{\dot{t} g_{rr}}. \quad (69)$$

Principal Lyapunov exponent can be defined as [68]

$$\sigma^2 = K_1 K_2, \quad (70)$$

For a circular geodesics, $V_r(r_c) = V'_r(r_c) = 0$ [69]. Thus, K_1 can be shown explicitly as

$$K_1 = \left. \left(\frac{1}{2g_{rr}\dot{t}} (g_{rr}^2 V_r)' \right)' \right|_{r=r_c}. \quad (71)$$

Here, we denote ' as derivative with respect to radial coordinate r . Thus, generic Lyapunov exponent for static spherically symmetric spacetime is obtained [67, 68]

$$\sigma = \sqrt{\left. \frac{V_r''}{2\dot{t}} \right|_{r=r_c}}. \quad (72)$$

Here, we consider only the positive sign of the Lyapunov exponent. From (65), the two conditions of circular null geodesics imply

$$\frac{E}{L} = \pm \sqrt{\frac{h_c}{r_c^2}}, \quad \text{and} \quad \frac{h'_c}{h_c} = \frac{2}{r_c}, \quad (73)$$

where $h(r_c) = r_c$. Finally, the Lyapunov exponent can be expressed explicitly as

$$\sigma = \sqrt{h_c \left(\frac{h_c}{r_c^2} - \frac{h''_c}{2} \right)}, \quad (74)$$

$$= \sqrt{\frac{(e^{\Delta} r_c - r_s) [(2r_c^2 - 4M_{DM}^2) (r_0 + r_c) + M_{DM} r_c (r_0 + 4r_c)]}{2e^{-\Delta} (r_0 + r_c) r_c^5}}. \quad (75)$$

For the sake of presentation, we simplify σ by using M_{DM} rather than the usual ρ_0 and introduce $\Delta \equiv \frac{4M_{DM}(r_0+r_c)}{r_0 r_c}$. In the absence of dark matter, $e^{\pm\Delta} = 1$, the Lyapunov exponent (75) reduce to $\sigma = \sqrt{\frac{r_c - r_s}{r_c^3}} = \frac{1}{3\sqrt{3}}$ which agrees with those of the Schwarzschild case [67]. The Lyapunov exponent denotes the inverse of the instability timescale between neighboring geodesics. The circular null geodesics is unstable when $\sigma > 0$. Clearly, (75) being real number signifies the instability of geodesics.

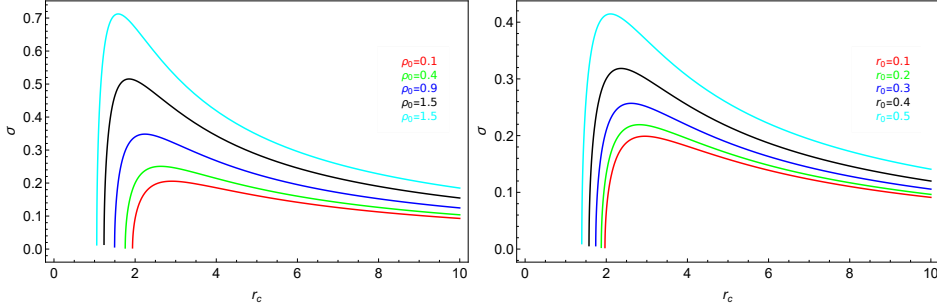


Fig. 15 The Lyapunov exponent as a function of r_c for various value of ρ_0 and r_0 . Left: fixed $r_0 = 0.1$ Right: fixed $\rho_0 = 0.05$.

As a demonstration, we display behaviour of the Lyapunov exponent σ in Fig. 15 for several cases of ρ_0 and r_0 . For each case, there exists a minimum value of r_c for which the Lyapunov exponent remains as real number. For instance, the Lyapunov exponent becomes complex number in $0 \leq r_c \leq 1.93$ for $\rho_0 = r_0 = 0.1$. We observe that increases in ρ_0 and r_0 generally lead to an overall increase in the magnitude of σ .

6 Eikonal Quasinormal Modes

Quasinormal modes (QNMs) characterize the damped oscillations of perturbations around a black hole or compact object, representing the system's natural response to external disturbances. Their complex frequencies have real parts corresponding to oscillation frequencies and imaginary parts describing decay rates, providing valuable insight into the stability and dynamical properties of the spacetime.

Let us consider a massive relativistic massless bosonic field perturbing the spherically symmetric black hole solution embedded in a Dehnen $(1, 4, \frac{3}{2})$ dark matter halo. The dynamics of the field are governed by the covariant Klein-Gordon equation, which in curved spacetime takes the form

$$\frac{1}{\sqrt{-g}} \partial_\mu (\sqrt{-g} g^{\mu\nu} \partial_\nu) \psi = 0, \quad (76)$$

where m is the mass of the bosonic field and g is the determinant of the metric tensor.

By substituting the explicit form of the metric given in (13) and following the procedure outlined in [70], we exploit the spherical symmetry of the spacetime and adopt the separation ansatz

$$\psi(t, r, \theta, \phi) = e^{-i\omega t} \frac{R(r)}{r} Y_\ell^{m_\ell}(\theta, \phi), \quad (77)$$

where $Y_\ell^{m_\ell}(\theta, \phi)$ are the standard spherical harmonics,

Using this ansatz, the Klein-Gordon equation reduces to a radial wave equation for $R(r)$,

$$\frac{d^2 R}{dr_*^2} + \left[\omega^2 - \frac{h}{r^2} \{ \ell(\ell+1) + rh' \} \right] R = 0, \quad (78)$$

where we have defined the tortoise coordinate

$$dr_* = \frac{dr}{h(r)}. \quad (79)$$

Equation (78) describes the radial propagation of scalar perturbations in the black hole–Dehnen halo spacetime, with the metric function $h(r)$ encoding the influence of both the central black hole and the surrounding dark matter distribution. Solving this equation with appropriate boundary conditions, i.e., purely ingoing wave at the horizon and purely outgoing wave at asymptotically infinity, allows us to determine the quasinormal mode frequencies. As a result, the corresponding frequencies are in the form of complex frequencies, i.e., $\omega = \omega_R \pm i\omega_I$.

To obtain the frequencies, there are several numerical approaches. However, there is an approximation that provides a useful analytical formula of quasinormal modes. We can consider geometric-optics or eikonal limit as proposed in [71–73]. In the eikonal limit, the QNM spectrum admits a clear geometric interpretation: the real part of the frequency corresponds to the angular velocity of the unstable circular photon orbit, while the imaginary part is determined by the Lyapunov exponent associated with the orbit’s instability [68]. This correspondence establishes a direct link between the classical motion of photons and the linear perturbative dynamics of the black hole. Analyzing eikonal QNMs therefore allows us to investigate how the parameters of the Dehnen halo influence both the oscillatory behavior and damping of perturbations in the black hole–dark matter system.

In the eikonal limit, where $l \gg 1$, the radial equation (78) simplifies considerably. Neglecting terms of order $\mathcal{O}(1)$ compared to l^2 , we obtain,

$$\partial_{r_*}^2 \mathcal{R}(r_*) + W(r) \mathcal{R}(r_*) = 0, \quad (80)$$

$$W(r) = \omega^2 - \frac{h}{r^2} l^2 = \omega^2 - l^2 V_{eff}. \quad (81)$$

To determine the quasinormal mode (QNM) frequencies in the eikonal regime, we employ the analytical first order WKB approximation. This semi-analytical method

provides an efficient and reliable way to estimate the complex frequencies associated with the effective potential barrier. The standard Iyer–Will WKB quantization condition is given by [74],

$$\frac{W(r_0)}{\sqrt{2W^{(2)}(r_0)}} = -i \left(n + \frac{1}{2} \right), \quad (82)$$

where $n = 0, 1, 2, \dots$ denotes the overtone number and,

$$W^{(2)}(r_0) = \left(\frac{d^2W}{dr_*^2} \right)_{r=r_0}. \quad (83)$$

The point r_0 corresponds to the extremum of both $W(r)$ and the effective potential $V_{eff}(r)$, consequently, $r_0 = r_{ph}$ is physically interpreted as the radius of the circular null orbit (or the photon sphere). The explicit expression of the WKB formula in (82) can be rewritten explicitly as

$$\omega_{QNM}^2 = \ell^2 V_{eff}(r_{ph}) - i \left(n + \frac{1}{2} \right) \sqrt{-2\ell^2 V_{eff}^{(2)}(r_{ph})}. \quad (84)$$

After taking square root and expanding for large ℓ , we obtain quasinormal frequency in a more transparent form as,

$$\omega_{QNM} \approx \ell \sqrt{V_{eff}(r_{ph})} - i \left(n + \frac{1}{2} \right) \sqrt{-\frac{V_{eff}^{(2)}(r_{ph})}{2V_{eff}(r_{ph})}}. \quad (85)$$

Now, let us evaluate the second derivative of the effective potential with respect to the tortoise coordinate. This is given by

$$\left(\frac{d^2V_{eff}}{dr_*^2} \right)_{r=r_{ph}} = \left[h(r) \frac{d}{dr} \left(h(r) \frac{dV_{eff}}{dr} \right) \right]_{r=r_{ph}} = h^2(r_{ph}) V_{eff}''(r_{ph}) \quad (86)$$

where $dV_{eff}/dr_* = 0|_{r=r_{ph}}$ is implemented. We find that V_{eff} is maximum at a radius satisfying $h'_{ph} = 2h_{ph}/r_{ph}$. By comparing with (73), we observe that r_{ph} coincides with circular null orbit r_c . Then, it is useful to consider

$$-\frac{V_{eff}^{(2)}(r_c)}{2V_{eff}(r_c)} = -\frac{1}{2} h_c \left(h_c'' - \frac{2h_c}{r_c^2} \right). \quad (87)$$

In comparison with (85), this allows us to rewrite (85) in term of the Lyapunov exponent

$$\omega_{QNM} = \ell \sqrt{\frac{h_c}{r_c^2}} - i \left(n + \frac{1}{2} \right) \sigma. \quad (88)$$

Interestingly, the real part of eikonal formula above has a connection to photon's critical impact parameter b_c and then to black hole's shadow radius via (51) and (52). It is also important to stress out that the imaginary part of the black hole's quasinormal mode spectrum is directly proportional to σ , which quantifies the stability or instability of the corresponding classical photon circular orbit. For a stable circular orbit, where $\sigma^2 < 0$, the quasinormal mode frequency ω_{QNM} is entirely real, indicating undamped oscillations. In contrast, an unstable circular orbit, for which $\sigma^2 > 0$, yields a complex ω_{QNM} with a negative imaginary part, corresponding to decaying perturbations and reflecting the intrinsic instability of the orbit.

For special case with $\rho_0 r_0^3 \ll 1$, we can perform series expansion and obtain,

$$\omega_{QNM} = \frac{2\ell}{3\sqrt{3}r_s^2} \left[r_s - \frac{16}{3}\pi\rho_0 r_0^2(r_0 - 3r_s) \right] - i \frac{2(n + \frac{1}{2})}{3\sqrt{3}r_s^2} \left[r_s - \frac{16}{3}\pi\rho_0 r_0^2(r_0 - 4r_s) \right] \quad (89)$$

For the Schwarzschild case, where $V_{eff} = \frac{1}{r^2} (1 - \frac{2M}{r})$ and $r_{ph} = 3M$, it is straightforward to compute $\sigma = \frac{1}{9M^2}$ and $V_{eff}(r_{ph}) = \frac{1}{27M^2}$. Substituting these values into the eikonal QNM formula, one recovers the well-known expression [71],

$$\omega_{QNM} = \frac{\ell}{3\sqrt{3}M} - i \frac{(n + \frac{1}{2})}{3\sqrt{3}M}. \quad (90)$$

This result clearly demonstrates how the general eikonal QNM expression reduces to the standard Schwarzschild limit, providing a useful consistency check for calculations involving more general black hole spacetimes, such as those embedded in a Dehnen dark matter halo.

7 Conclusion

In this work, we construct and analyze a new static, spherically symmetric black hole solution embedded in a Dehnen $(1, 4, \frac{3}{2})$ dark matter halo. The Dehnen profile has been widely used in astrophysics to model elliptical galaxies and bulges, but its influence on black hole solutions has yet to be fully investigated. By embedding a Schwarzschild black hole in this density distribution, we can obtain an exact analytic form of the metric and investigate how the halo affects spacetime structure. The halo parameters, ρ_0 and r_0 , have a significant impact on the horizon location and curvature invariants, while maintaining the essential singularity at the origin, according to the mass distribution and metric functions.

We then look at the energy conditions of the combined black hole-halo spacetime. Our findings indicate that, while the strong energy condition is generally met, both the weak and dominant energy conditions are violated. Some combinations of ρ_0 and r_0 can satisfy the null energy condition, but only outside the horizon. These findings highlight the nontrivial behavior of the energy-momentum tensor produced by the Dehnen halo, implying that the halo's effective stress-energy may mimic exotic matter properties in curved spacetime.

The thermodynamic properties of the system are also investigated. We construct the black hole mass function and derive analytical functions for entropy, Hawking

temperature, heat capacity and Gibbs free energy. Unlike the Schwarzschild case, which is always thermodynamically unstable, the presence of a Dehnen halo creates regions with positive heat capacity, indicating local stability. Furthermore, the system experiences second-order phase transitions, as evidenced by discontinuities in heat capacity while entropy remains constant. The Gibbs free energy analysis also reveals that higher halo density and larger core radius improve the global stability of the system by minimizing the positive Gibbs free energy region, demonstrating that dark matter can act as a stabilizing medium for black holes.

We explore the observable shadow of the black hole encircled by the Dehnen halo and null geodesics. Depending on the halo parameters, the photons' effective potential shows changes to the photon sphere and circular orbits. The apparent shadow radius and the critical impact parameter are directly impacted by these modifications. Our computations indicate that the shadow size grows with scale radius and halo density, pointing to possible dark matter observational signatures in black hole imaging. Additionally, weak gravitational lensing is examined, demonstrating that the halo considerably modifies light deflection at low impact parameters. These findings provide a useful framework for relating theoretical models with astrophysical observations by demonstrating that embedding a black hole in a Dehnen-type dark matter halo results in unique thermodynamic and optical signatures.

Furthermore, we clarify how the dynamics of photon orbits are reflected in the spacetime's response to perturbations. We analytically show that the Lyapunov exponent describing the instability of circular photon orbits is directly linked to the imaginary part of the massless quasinormal mode frequencies in the eikonal limit, which set the decay times of relativistic perturbations. We find that increasing both ρ_0 and r_0 increases the divergence rate of two nearby orbits. This result emphasizes the photon sphere as the key structure connecting black hole shadows, gravitational lensing and quasinormal ringing. Consequently, when a Schwarzschild black hole is embedded in the Dehnen $(1, 4, \frac{3}{2})$ dark matter halo, changes in the photon orbit instability leave simultaneous imprints on both optical observables and the damping of perturbations, offering a complementary way to probe the surrounding dark matter environment.

As a further extension, a comprehensive analysis of the optical appearance of a black hole embedded in a Dehnen dark matter halo would be highly valuable. In particular, calculating the resulting shadow, lensing features, and associated observables in this composite spacetime could provide an astrophysical probe of the Dehnen halo parameters. Such a study may help constrain the structure and distribution of Dehnen-type dark matter halos through comparison with high-resolution imaging and lensing data. Research in this direction is currently underway.

Acknowledgment

TC and SP acknowledge funding support from the NSRF via the Program Management Unit for Human Resource and Institutional Development, Research and Innovation grant number *B39G680009*.

References

- [1] Abbott, B.P., *et al.*: Properties of the Binary Black Hole Merger GW150914. *Phys. Rev. Lett.* **116**(24), 241102 (2016) <https://doi.org/10.1103/PhysRevLett.116.241102> arXiv:1602.03840 [gr-qc]
- [2] Akiyama, K., *et al.*: First M87 Event Horizon Telescope Results. VI. The Shadow and Mass of the Central Black Hole. *Astrophys. J. Lett.* **875**(1), 6 (2019) <https://doi.org/10.3847/2041-8213/ab1141> arXiv:1906.11243 [astro-ph.GA]
- [3] Akiyama, K., *et al.*: First Sagittarius A* Event Horizon Telescope Results. I. The Shadow of the Supermassive Black Hole in the Center of the Milky Way. *Astrophys. J. Lett.* **930**(2), 12 (2022) <https://doi.org/10.3847/2041-8213/ac6674> arXiv:2311.08680 [astro-ph.HE]
- [4] Rubin, V.C., Ford, W.K. Jr.: Rotation of the Andromeda Nebula from a Spectroscopic Survey of Emission Regions. *Astrophys. J.* **159**, 379–403 (1970) <https://doi.org/10.1086/150317>
- [5] Massey, R., Kitching, T., Richard, J.: The dark matter of gravitational lensing. *Rept. Prog. Phys.* **73**, 086901 (2010) <https://doi.org/10.1088/0034-4885/73/8/086901> arXiv:1001.1739 [astro-ph.CO]
- [6] Aghanim, N., *et al.*: Planck 2018 results. VI. Cosmological parameters. *Astron. Astrophys.* **641**, 6 (2020) <https://doi.org/10.1051/0004-6361/201833910> arXiv:1807.06209 [astro-ph.CO]. [Erratum: *Astron. Astrophys.* 652, C4 (2021)]
- [7] Clowe, D., Gonzalez, A., Markevitch, M.: Weak lensing mass reconstruction of the interacting cluster 1E0657-558: Direct evidence for the existence of dark matter. *Astrophys. J.* **604**, 596–603 (2004) <https://doi.org/10.1086/381970> arXiv:astro-ph/0312273
- [8] Markevitch, M., Gonzalez, A.H., Clowe, D., Vikhlinin, A., David, L., Forman, W., Jones, C., Murray, S., Tucker, W.: Direct constraints on the dark matter self-interaction cross-section from the merging galaxy cluster 1E0657-56. *Astrophys. J.* **606**, 819–824 (2004) <https://doi.org/10.1086/383178> arXiv:astro-ph/0309303
- [9] Gebhardt, K., Adams, J., Richstone, D., Lauer, T.R., Faber, S.M., Gultekin, K., Murphy, J., Tremaine, S.: The Black-Hole Mass in M87 from Gemini/NIFS Adaptive Optics Observations. *Astrophys. J.* **729**, 119 (2011) <https://doi.org/10.1088/0004-637X/729/2/119> arXiv:1101.1954 [astro-ph.CO]
- [10] Mathew, S.: Essays on the Frontiers of Modern Astrophysics and Cosmology. Springer Praxis Books. Springer, ??? (2014). link.springer.com
- [11] Fidler, W.: Dark Matter. New Structures, Old Particles. GRIN Verlag, ??? (2018). <https://books.google.co.th/books?id=jdFiDwAAQBAJ>

- [12] Wechsler, R.H., Tinker, J.L.: The Connection between Galaxies and their Dark Matter Halos. *Ann. Rev. Astron. Astrophys.* **56**, 435–487 (2018) <https://doi.org/10.1146/annurev-astro-081817-051756> arXiv:1804.03097 [astro-ph.GA]
- [13] Jusufi, K., Jamil, M., Salucci, P., Zhu, T., Haroon, S.: Black hole surrounded by a dark matter halo in the m87 galactic center and its identification with shadow images. *Phys. Rev. D* **100**, 044012 (2019) <https://doi.org/10.1103/PhysRevD.100.044012>
- [14] Konoplya, R.A., Zhidenko, A.: Solutions of the Einstein Equations for a Black Hole Surrounded by a Galactic Halo. *Astrophys. J.* **933**(2), 166 (2022) <https://doi.org/10.3847/1538-4357/ac76bc> arXiv:2202.02205 [gr-qc]
- [15] Figueiredo, E., Maselli, A., Cardoso, V.: Black holes surrounded by generic dark matter profiles: Appearance and gravitational-wave emission. *Phys. Rev. D* **107**(10), 104033 (2023) <https://doi.org/10.1103/PhysRevD.107.104033> arXiv:2303.08183 [gr-qc]
- [16] Liu, D., Yang, Y., Xu, Z., Long, Z.-W.: Modeling the black holes surrounded by a dark matter halo in the galactic center of M87. *Eur. Phys. J. C* **84**(2), 136 (2024) <https://doi.org/10.1140/epjc/s10052-024-12492-4> arXiv:2307.13553 [gr-qc]
- [17] Xavier, S.V.M.C.B., Lima, H.C.D. Junior., Crispino, L.C.B.: Shadows of black holes with dark matter halo. *Phys. Rev. D* **107**(6), 064040 (2023) <https://doi.org/10.1103/PhysRevD.107.064040> arXiv:2303.17666 [gr-qc]
- [18] Jha, S.K.: Thermodynamics, weak gravitational lensing, and parameter estimation of a Schwarzschild black hole immersed in Hernquist dark matter halo. *JCAP* **06**, 033 (2025) <https://doi.org/10.1088/1475-7516/2025/06/033> arXiv:2503.19938 [gr-qc]
- [19] Kar, A., Kar, S.: Diverse regular spacetimes using a parametrised density profile. *Eur. Phys. J. C* **85**(7), 773 (2025) <https://doi.org/10.1140/epjc/s10052-025-14483-5> arXiv:2504.12042 [gr-qc]
- [20] Dehnen, W.: A family of potential–density pairs for spherical galaxies and bulges. *Monthly Notices of the Royal Astronomical Society* **265**(1), 250–256 (1993) <https://doi.org/10.1093/mnras/265.1.250>
- [21] Hickox, R., Parker, J., Smith, S., Ananna, T.T.: Uncovering a Hidden Mini-Monster: A Heavily Obscured AGN in a Dwarf Star-forming Galaxy. In: *AAS/High Energy Astrophysics Division*, vol. 19, pp. 106–35 (2022)
- [22] Schutte, Z., Reines, A.E.: Black-hole-triggered star formation in the dwarf galaxy Henize 2-10. *Nature* **601**(7893), 329–333 (2022) <https://doi.org/10.1038/s41586-021-04215-6> arXiv:2201.08396 [astro-ph.GA]

- [23] Bustamante-Rosell, M.J., Noyola, E., Gebhardt, K., Fabricius, M.H., Mazzalay, X., Thomas, J., Zeimann, G.: Dynamical analysis of the dark matter and central black hole mass in the dwarf spheroidal leo i. *The Astrophysical Journal* **921**(2), 107 (2021) <https://doi.org/10.3847/1538-4357/ac0c79>
- [24] Pantig, R.C., Övgün, A.: Dehnen halo effect on a black hole in an ultra-faint dwarf galaxy. *JCAP* **08**(08), 056 (2022) <https://doi.org/10.1088/1475-7516/2022/08/056> [arXiv:2202.07404](https://arxiv.org/abs/2202.07404) [astro-ph.GA]
- [25] Gohain, M.M., Phukon, P., Bhuyan, K.: Thermodynamics and null geodesics of a Schwarzschild black hole surrounded by a Dehnen type dark matter halo. *Phys. Dark Univ.* **46**, 101683 (2024) <https://doi.org/10.1016/j.dark.2024.101683> [arXiv:2407.02872](https://arxiv.org/abs/2407.02872) [gr-qc]
- [26] Al-Badawi, A., Shaymatov, S., Sekhmani, Y.: Schwarzschild black hole in galaxies surrounded by a dark matter halo. *JCAP* **02**, 014 (2025) <https://doi.org/10.1088/1475-7516/2025/02/014> [arXiv:2411.01145](https://arxiv.org/abs/2411.01145) [gr-qc]
- [27] Toshmatov, B., Ahmedov, B., Boydedayev, A., Ahmedov, B.: Dynamics of black hole in dark matter halo: Quasinormal modes. *Phys. Rev. D* **111**(12), 124058 (2025) <https://doi.org/10.1103/physrevd.111.124058>
- [28] Uktamov, U., Shaymatov, S., Ahmedov, B.: Static black hole solution with a dark matter halo (2025) [arXiv:2505.20031](https://arxiv.org/abs/2505.20031) [gr-qc]
- [29] Senjaya, D.: Black hole in Dehnen $(1, 4, \frac{1}{2})$ dark matter halo: exact solution, lensing, light ring, and thermodynamics. *Eur. Phys. J. C* **85**(11), 1256 (2025) <https://doi.org/10.1140/epjc/s10052-025-15005-z>
- [30] Xu, Z., Hou, X., Gong, X., Wang, J.: Black Hole Space-time In Dark Matter Halo. *JCAP* **09**, 038 (2018) <https://doi.org/10.1088/1475-7516/2018/09/038> [arXiv:1803.00767](https://arxiv.org/abs/1803.00767) [gr-qc]
- [31] Rani, S., Jawad, A., Heydari-Fard, M., Zafar, U.: Thermodynamic and shadow analysis of Dehnen type dark matter Halo corrected Schwarzschild black hole surrounded by thin disk. *Eur. Phys. J. C* **85**(6), 677 (2025) <https://doi.org/10.1140/epjc/s10052-025-14388-3>
- [32] Mo, H., Bosch, F., White, S.: *Galaxy Formation and Evolution*. Cambridge University Press, Cambridge (2010)
- [33] Toshmatov, B., Bambi, C., Ahmedov, B., Abdujabbarov, A., Stuchlík, Z.: Energy conditions of non-singular black hole spacetimes in conformal gravity. *Eur. Phys. J. C* **77**(8), 542 (2017) <https://doi.org/10.1140/epjc/s10052-017-5112-2> [arXiv:1702.06855](https://arxiv.org/abs/1702.06855) [gr-qc]
- [34] Nicolini, P., Smailagic, A., Spallucci, E.: Noncommutative geometry inspired

Schwarzschild black hole. *Phys. Lett. B* **632**, 547–551 (2006) <https://doi.org/10.1016/j.physletb.2005.11.004> arXiv:gr-qc/0510112

[35] Ansoldi, S., Nicolini, P., Smailagic, A., Spallucci, E.: Noncommutative geometry inspired charged black holes. *Phys. Lett. B* **645**, 261–266 (2007) <https://doi.org/10.1016/j.physletb.2006.12.020> arXiv:gr-qc/0612035

[36] Neves, J.C.S., Saa, A.: Regular rotating black holes and the weak energy condition. *Phys. Lett. B* **734**, 44–48 (2014) <https://doi.org/10.1016/j.physletb.2014.05.026> arXiv:1402.2694 [gr-qc]

[37] Zhang, H.-X., Chen, Y., Ma, T.-C., He, P.-Z., Deng, J.-B.: Bardeen black hole surrounded by perfect fluid dark matter. *Chin. Phys. C* **45**(5), 055103 (2021) <https://doi.org/10.1088/1674-1137/abe84c> arXiv:2007.09408 [gr-qc]

[38] Tangphati, T., Youk, M., Ponglertsakul, S.: Magnetically charged regular black holes in f(R,T) gravity coupled to nonlinear electrodynamics. *JHEAp* **43**, 66–78 (2024) <https://doi.org/10.1016/j.jheap.2024.06.009> arXiv:2312.16614 [gr-qc]

[39] Sajadi, S.N., Ponglertsakul, S., Luongo, O.: Constructing black holes from multi-polytropic equations of state. *Phys. Dark Univ.* **48**, 101938 (2025) <https://doi.org/10.1016/j.dark.2025.101938> arXiv:2502.02098 [gr-qc]

[40] Khan, S., Rayimbaev, J., Ibragimov, I., Muminov, S., Dauletov, A.: Einasto-inspired non-commutative black holes within dark matter galactic halos in f(Q) gravity. *Annals Phys.* **481**, 170130 (2025) <https://doi.org/10.1016/j.aop.2025.170130>

[41] Stelea, C., Dariescu, M.-A., Dariescu, C.: Charged black holes with dark halos. *Physics Letters B* **847**, 138275 (2023) <https://doi.org/10.1016/j.physletb.2023.138275> arXiv:2309.13651 [gr-qc]

[42] Myung, Y.S.: Thermodynamic analysis and shadow bound of black holes surrounded by a dark matter halo. *European Physical Journal C* **85**(10), 1116 (2025) <https://doi.org/10.1140/epjc/s10052-025-14861-z> arXiv:2502.13397 [gr-qc]

[43] Kastor, D., Ray, S., Traschen, J.: Enthalpy and the Mechanics of AdS Black Holes. *Class. Quant. Grav.* **26**, 195011 (2009) <https://doi.org/10.1088/0264-9381/26/19/195011> arXiv:0904.2765 [hep-th]

[44] Kastor, D., Ray, S., Traschen, J.: Black Hole Enthalpy and Scalar Fields. *Class. Quant. Grav.* **36**(2), 024002 (2019) <https://doi.org/10.1088/1361-6382/aaf663> arXiv:1807.09801 [gr-qc]

[45] Bekenstein, J.D.: Black holes and entropy. *Phys. Rev. D* **7**, 2333–2346 (1973) <https://doi.org/10.1103/PhysRevD.7.2333>

[46] Mann, R.B.: Black hole chemistry: The first 15 years. *Int. J. Mod. Phys. D* **34**(09), 2542001 (2025) <https://doi.org/10.1142/S0218271825420015> arXiv:2508.01830 [gr-qc]

[47] Singh, D.V., Upadhyay, S., Myrzakulov, Y., Myrzakulov, K., Singh, B., Kumar, M.: Thermodynamic behavior and phase transitions of black holes with a cloud of strings and perfect fluid dark matter. *Nucl. Phys. B* **1016**, 116915 (2025) <https://doi.org/10.1016/j.nuclphysb.2025.116915>

[48] Kachelriess, M.: Quantum Fields: From the Hubble to the Planck Scale. Oxford Graduate Texts. Oxford University Press, ??? (2017). <https://doi.org/10.1093/oso/9780198802877.001.0001>

[49] Benkrane, A., Zenkhri, D.E.: Impact of dark matter halo on black hole: Thermodynamical properties and photons motion. *Nucl. Phys. B* **1018**, 117069 (2025) <https://doi.org/10.1016/j.nuclphysb.2025.117069>

[50] Nolting, W.: Theoretical Physics 5, (2017). <https://doi.org/10.1007/978-3-319-47910-1>

[51] Roychowdhury, D.: Phase transition in black holes (2014). <https://arxiv.org/abs/1403.4356>

[52] Rostami, M., Sadeghi, J., Miraboutalebi, S.: The static black hole in $f(R)$ gravity with thermal corrections and phase transition. *Phys. Dark Univ.* **29**, 100590 (2020) <https://doi.org/10.1016/j.dark.2020.100590>

[53] Grenzebach, A.: The Shadow of Black Holes: An Analytic Description. Springer-Briefs in Physics. Springer, ??? (2016). https://books.google.co.th/books?id=0_MgDAAAQBAJ

[54] Pantig, R.C.: Apparent and emergent dark matter around a Schwarzschild black hole. *Phys. Dark Univ.* **45**, 101550 (2024) <https://doi.org/10.1016/j.dark.2024.101550> arXiv:2405.07531 [gr-qc]

[55] Perlick, V., Tsupko, O.Y.: Calculating black hole shadows: Review of analytical studies. *Phys. Rept.* **947**, 1–39 (2022) <https://doi.org/10.1016/j.physrep.2021.10.004> arXiv:2105.07101 [gr-qc]

[56] Kocherlakota, P., *et al.*: Constraints on black-hole charges with the 2017 EHT observations of M87*. *Phys. Rev. D* **103**(10), 104047 (2021) <https://doi.org/10.1103/PhysRevD.103.104047> arXiv:2105.09343 [gr-qc]

[57] Akiyama, K., *et al.*: First Sagittarius A* Event Horizon Telescope Results. VI. Testing the Black Hole Metric. *Astrophys. J. Lett.* **930**(2), 17 (2022) <https://doi.org/10.3847/2041-8213/ac6756> arXiv:2311.09484 [astro-ph.HE]

[58] Vagnozzi, S., *et al.*: Horizon-scale tests of gravity theories and fundamental physics from the Event Horizon Telescope image of Sagittarius A. *Class. Quant. Grav.* **40**(16), 165007 (2023) <https://doi.org/10.1088/1361-6382/acd97b> arXiv:2205.07787 [gr-qc]

[59] Javed, W., Riaz, S., Övgün, A.: Weak Deflection Angle and Greybody Bound of Magnetized Regular Black Hole. *Universe* **8**(5), 262 (2022) <https://doi.org/10.3390/universe8050262> arXiv:2205.02229 [gr-qc]

[60] Gibbons, G.W., Werner, M.C.: Applications of the Gauss-Bonnet theorem to gravitational lensing. *Class. Quant. Grav.* **25**, 235009 (2008) <https://doi.org/10.1088/0264-9381/25/23/235009> arXiv:0807.0854 [gr-qc]

[61] Waseem, H., Lobos, N.J.L.S., Övgün, A., Pantig, R.C.: Analyzing deflection angles and photon sphere dynamics of magnetically charged black holes in nonlinear electrodynamic. *Eur. Phys. J. C* **85**(6), 629 (2025) <https://doi.org/10.1140/epjc/s10052-025-14373-w> arXiv:2502.04044 [gr-qc]

[62] Mandal, S.: Weak deflection angle, Hawking radiation, greybody bound and shadow cast for static black hole in the framework of f(R) gravity. *Phys. Dark Univ.* **42**, 101374 (2023) <https://doi.org/10.1016/j.dark.2023.101374> arXiv:2309.16461 [gr-qc]

[63] Panpanich, S., Ponglertsakul, S., Tannukij, L.: Particle motions and Gravitational Lensing in de Rham-Gabadadze-Tolley Massive Gravity Theory. *Phys. Rev. D* **100**(4), 044031 (2019) <https://doi.org/10.1103/PhysRevD.100.044031> arXiv:1904.02915 [gr-qc]

[64] Pantig, R.C., Övgün, A.: Dark matter effect on the weak deflection angle by black holes at the center of Milky Way and M87 galaxies. *Eur. Phys. J. C* **82**(5), 391 (2022) <https://doi.org/10.1140/epjc/s10052-022-10319-8> arXiv:2201.03365 [gr-qc]

[65] Liu, Y.-G., Qiao, C.-K., Tao, J.: Gravitational lensing of spherically symmetric black holes in dark matter halos. *Journal of Cosmology and Astroparticle Physics* **2024**, 075 (2024) <https://doi.org/10.1088/1475-7516/2024/10/075>

[66] Molla, N.U., Chaudhary, H., Capozziello, S., Atamurotov, F., Mustafa, G., Debnath, U.: Observable signatures of RN black holes with dark matter halos via strong gravitational lensing and constraints from EHT observations. *Phys. Dark Univ.* **47**, 101804 (2025) <https://doi.org/10.1016/j.dark.2024.101804> arXiv:2501.09439 [gr-qc]

[67] Mondal, M., Pradhan, P., Rahaman, F., Karar, I.: Geodesic stability and Quasi normal modes via Lyapunov exponent for Hayward Black Hole. *Mod. Phys. Lett. A* **35**(30), 2050249 (2020) <https://doi.org/10.1142/S0217732320502491> arXiv:2008.11022 [gr-qc]

- [68] Cardoso, V., Miranda, A.S., Berti, E., Witek, H., Zanchin, V.T.: Geodesic stability, Lyapunov exponents and quasinormal modes. *Phys. Rev. D* **79**(6), 064016 (2009) <https://doi.org/10.1103/PhysRevD.79.064016> arXiv:0812.1806 [hep-th]
- [69] Bardeen, J.M., Press, W.H., Teukolsky, S.A.: Rotating black holes: Locally nonrotating frames, energy extraction, and scalar synchrotron radiation. *Astrophysical Journal* **178**, 347–370 (1972)
- [70] Senjaya, D., Ponglertsakul, S.: The extreme Reissner–Nordström Black Hole: New exact solutions to the Klein–Gordon equation with minimal coupling. *Annals Phys.* **473**, 169898 (2025) <https://doi.org/10.1016/j.aop.2024.169898> arXiv:2405.07579 [gr-qc]
- [71] Ferrari, V., Mashhoon, B.: New approach to the quasinormal modes of a black hole. *Phys. Rev. D* **30**, 295–304 (1984) <https://doi.org/10.1103/PhysRevD.30.295>
- [72] Mashhoon, B.: Stability of charged rotating black holes in the eikonal approximation. *Phys. Rev. D* **31**(2), 290–293 (1985) <https://doi.org/10.1103/PhysRevD.31.290>
- [73] Mashhoon, B.: Erratum: Stability of charged rotating black holes in the eikonal approximation. *Phys. Rev. D* **31**, 2697–2697 (1985) <https://doi.org/10.1103/PhysRevD.31.2697.2>
- [74] Schutz, B.F., Will, C.M.: BLACK HOLE NORMAL MODES: A SEMIANALYTIC APPROACH. *Astrophys. J. Lett.* **291**, 33–36 (1985) <https://doi.org/10.1086/184453>